Review

Cell PRESS

Feature Review

Structure, dynamics and biophysics of the cytoplasmic protein–protein complexes of the bacterial phosphoenolpyruvate: sugar phosphotransferase system

G. Marius Clore and Vincenzo Venditti

Laboratory of Chemical Physics, National Institute of Diabetes and Digestive and Kidney Diseases, National Institutes of Health, Bethesda, MD 20892-0520, USA

The bacterial phosphotransferase system (PTS) couples phosphoryl transfer, via a series of bimolecular protein–protein interactions, to sugar transport across the membrane. The multitude of complexes in the PTS provides a paradigm for studying protein interactions, and for understanding how the same binding surface can specifically recognize a diverse array of targets. Fifteen years of work aimed at solving the solution structures of all soluble protein–protein complexes of the PTS has served as a test bed for developing NMR and integrated hybrid approaches to study larger complexes in solution and to probe transient, spectroscopically invisible states, including encounter complexes. We review these approaches, highlighting the problems that can be tackled with these methods, and summarize the current findings on protein interactions.

The PTS as a paradigm for understanding complex protein interactions

The bacterial phosphoenolpyruvate: sugar phosphotransferase system (PTS) is the key signal transduction pathway involved in the regulation of central carbon metabolism in bacteria [1–7]. The PTS comprises a sequential cascade of bimolecular protein–protein complexes whereby a phosphoryl group originating on phosphoenolpyruvate (PEP) is transferred onto incoming sugars, thereby coupling phosphoryl transfer to active sugar transport across the membrane. The first two steps of the PTS are common to all sugars: Enzyme I (EI) is autophosphorylated by PEP and subsequently transfers the phosphoryl group to the histidine phosphocarrier protein HPr. HPr donates the phosphoryl group to the A component of the sugar-specific Enzymes II. There are four classes of Enzymes II: glucose (the first branch of the PTS to have been discovered in 1964 [1]), mannitol, mannose, and lactose/chitobiose (Figure 1A). The organization of the sugar-specific Enzymes II is similar: there are two cytoplasmic domains, IIA and IIB, and a transmembrane domain IIC, which may be supplemented by a fourth transmembrane domain IID. These domains may occur either as isolated proteins or be covalently joined by long linkers in a single contiguous protein (Figure 1A). IIA accepts the phosphoryl group from HPr and donates it to IIB; finally the transmembrane domain IIC catalyzes the coupled translocation and phosphoryl transfer from IIB to the incoming sugar. Despite the similar organization of Enzymes II, the IIA domains from the four sugar classes bear no similarity to one another in terms of sequence, or secondary, tertiary, or quaternary structure [8–14]. The IIB domains from the mannitol [15,16] and chitobiose [17,18] branches are similar in terms of secondary and tertiary structure but have no significant sequence similarity outside of the active site loop. The active site loop of the IIB domain of the glucose branch [19] bears some similarities to that of the IIB domains from the mannitol and chitobiose branches, but displays no overall similarity in sequence, or secondary or tertiary structure. Lastly the IIB domain of the mannose pathway [20–22] bears no similarity at all to that of the other three branches.

In addition to their function within the PTS cascade, components of the PTS are also involved in the regulation of many other proteins, including glycogen phosphorylase, adenylate kinase, glycerol kinase, various non-PTS permeases, and the global repressor Mlc [3,7,23–27]. In addition, under conditions of nitrogen limitation, competitive inhibition of EI by α-ketoglutarate [28], the carbon substrate for ammonia assimilation, blocks sugar transfer across the cell membrane, thereby providing a direct

Corresponding author: Clore, G.M. (mariusc@mail.nih.gov).

Keywords: signal transduction; protein–protein recognition; bacterial phosphotransferase system; NMR spectroscopy; hybrid methods in structure determination; residual dipolar couplings; solution X-ray scattering; sparsely populated states; encounter complexes.

0968-0004/$ – see front matter.
Published by Elsevier Ltd. http://dx.doi.org/10.1016/j.tibs.2013.08.003

Glossary

Heteronuclear NMR: NMR experiments that make use of correlations between different types of NMR active nuclei, such as ^{1}H, ^{15}N, and ^{13}C.

Multidimensional NMR: Experiments that correlate chemical shifts in several dimensions. For example, a 2D ^{1}H-^{15}N correlation experiment correlates the chemical shift of a backbone amide proton with the ^{15}N shift of its directly bonded nitrogen atom via the one-bond ^{1}H-^{15}N scalar coupling. A 2D experiment comprises a preparation pulse, an evolution period during which the nuclear spins are labeled according to their chemical shifts, a mixing period during which the spins are correlated to one another (e.g., through-bond via scalar couplings or through space via the nuclear Overhauser effect), and a detection period. A 3D experiment that correlates chemical shifts in three dimensions is constructed from two 2D experiments by leaving out the detection period of the first 2D experiment and the preparation pulse of the second 2D experiment. Similarly, extension to a 4D experiment which correlates chemical shifts in four dimensions is constructed by combining a 3D experiment with a 2D one using exactly the same procedure.

Nuclear Overhauser effect (NOE): The NOE detects through-space interactions between protons separated by less than 5 Å and constitutes the mainstay of traditional NMR protein structure determination.

Relaxation dispersion spectroscopy: This is a class of NMR experiment designed to analyze exchange dynamics in the submillisecond to millisecond time scale that is dependent upon differences in chemical shifts between the species. The technique is capable of detecting exchange between an NMR visible major species and a spectroscopically invisible species populated as little as 1%. The experiment yields exchange rates, populations and the chemical shift differences between the species.

Residual dipolar couplings (RDC): RDCs are measured by taking the difference in scalar couplings recorded in aligned and isotropic (i.e., water) media. Examples of aligned media are bicelles and phage. These alignment media generate a very weak force on the protein that results in a small degree of alignment with respect to the magnetic field. As a result dipolar couplings between nuclei, as well as other orientation-dependent interactions, are no longer averaged to zero through Brownian rotational diffusion. The size of the RDC between two directly bonded nuclei is related to the orientation of the vector connecting the two nuclei to the alignment tensor.

Solution X-ray scattering: Small (SAXS) and wide (WAXS) angle X-ray scattering yield 1D profiles of scattering intensity as a function of the scattering vector q (given by $4\pi \sin\theta/\lambda$; where 2θ is the angle between the incident beam and the detector and λ the wavelength of the X-rays) [83]. The scattering profiles are determined by the pairwise distances between all atoms in a molecule and therefore contain information on molecular shape and size. Because of the convoluted nature of SAXS/WAXS it is not possible, outside of the very low q range, to extract features of the scattering curve to a particular structure, and it is generally not feasible to derive unique 3D structures from 1D profiles as many models may be compatible with a particular scattering profile. However, direct refinement against SAXS/WAXS data in combination with other experimental restraints, such as those from NMR can be extremely powerful [40,41,88–90].

Small angle neutron scattering (SANS): The principals of SANS are the same as those for SAXS/WAXS except neutrons instead of X-rays are used. The values of the atomic and solvent scattering amplitudes are different for SAXS/WAXS and SANS; therefore, the two techniques provide complementary information so that SANS can be used to validate the results of refinement against SAXS/WAXS. Furthermore, contrast- matched SANS on protein complexes in 40.4% D_2O in which one component is protonated and the other deuterated enables one to selectively record SANS profiles originating from only one component of the complex.

biochemical link between central nitrogen and carbon metabolism in bacteria [29].

Many reviews have been written on the biology of the PTS and on the structures of individual components of the PTS [2–7]. Although crystal structures [8–13,17,21,22,30–35] have been solved for many of the cytoplasmic isolated proteins or domains of the PTS (the remainder being solved by NMR [14–16,18–20,36–41]), crystallization of PTS complexes has proved refractory. This is largely due to the fact that the complexes are transient and rather weak with equilibrium dissociation constants (K_d) ranging from micro- to millimolar. Fortunately, this is not an impediment to the structure determination of such complexes in solution by NMR.

The multiplicity of protein–protein interactions in the PTS provides a paradigm for studying the factors governing specific recognition of multiple diverse targets. The current review focuses specifically on the NMR work in our laboratory, initiated in 1997 with the structure determination of the N-terminal domain of EI [39], aimed at understanding the structural basis of specific protein–protein recognition within the PTS; the fundamental biophysical mechanisms underlying protein–protein interactions; and the nature of large conformational rearrangements in multidomain proteins. In terms of structural biology and biophysics, these studies of protein–protein complexes of the PTS have provided a test bed for developing hybrid methods for solving the structures of large complexes and proteins in solution combining NMR and, in some instances, solution X-ray scattering, with crystal or NMR structures of individual domains, and for developing NMR methods for detecting and characterizing sparsely populated, transient encounter complexes formed by random collisions between partner proteins that precede the formation of the specific complex.

Solving the 3D solution structures of PTS complexes

The first structure of a PTS protein–protein complex to be determined was that between the N-terminal domain of EI (EIN) and HPr [42], for which the traditional approach involving a complete NMR structure determination of the entire complex was used (Box 1). It was rapidly realized, however, that this time-consuming approach could be both speeded up and rendered more accurate by making use of the available crystal or NMR structures of the free proteins [43]. This assumes that the backbone conformation of the proteins undergoes minimal changes upon complex formation, which can be readily ascertained both from the measurement of residual dipolar couplings (RDCs; see Glossary) as well as the observation of small backbone chemical shift changes upon complexation. The remainder of the PTS complexes were therefore solved by a procedure known as conjoined rigid body/torsion angle simulated annealing (Box 2), in which the proteins are treated as rigid bodies that are free to translate and rotate relative to one another, and interfacial side chains are given torsional degrees of freedom [43,44]. The driving force for these calculations resides in intermolecular nuclear Overhauser enhancement (NOE)-derived interproton distance restraints combined, where possible, with RDCs to provide orientational restraints and heteronuclear scalar couplings to derive torsion angle restraints for the interfacial side chains. This approach does not require that the complete backbone be treated as a rigid body: if there is evidence that a region of the backbone undergoes a conformational change upon complexation, then it is a simple matter to give that region torsional degrees of freedom whose conformational space is dictated by experimental NMR restraints (NOEs and RDCs measured on the complex) [45].

Whether one chooses to do a full NMR structure determination or to make use of known structures of the free protein, it is essential to distinguish unambiguously intermolecular NOEs from intramolecular NOEs within the individual proteins. This is readily accomplished by making use of appropriate isotopic labeling of the individual proteins [46]. For example, by ^{13}C labeling one protein and having the other protein at natural isotopic abundance one

Box 1. Brief overview of NMR structure determination

Traditionally, the geometric information used to solve 3D NMR structures of macromolecules relies principally on short (<6 Å) interproton distances derived from NOE measurements [91,92]. Many protons that are close in space are far apart in sequence, and hence, short interproton distance restraints are conformationally restrictive and sufficient, in their own right, to determine a 3D structure. Loose distance restraints, typically ranging from 1.8 to 2.7 Å, 1.8 to 3.5 Å, 1.8 to 5 Å, and 1.8 to 6 Å, corresponding to strong, medium, weak, and very weak NOEs, are adequate. Indeed, attempts to make use of more precise interproton distance restraints can often lead to a reduction in accuracy, owing to a phenomenon known as spin diffusion, whereby an NOE from say proton *i* to proton *j* is subsequently transferred to other protons in close proximity to proton *j* but far (>5 Å) from proton *i*. Supplementary structural restraints on backbone torsion angles can be obtained from three-bond scalar couplings [93] and backbone chemical shifts [94]. However, NOE and torsion angle restraints are short range in nature as they require close spatial proximity of the relevant atoms, and are therefore not good at specifying long-range order.

Long-range information can be obtained from RDCs measured in a dilute liquid crystalline medium [95,96] such as bicelles [97] or phage pf1 [98]. These media induce a small degree ($\sim 10^{-3}$) of alignment with respect to the magnetic field such that linewidths remain narrow but internuclear dipolar couplings are no longer averaged to zero by Brownian rotational diffusion. The value of an RDC (D) for an interatomic vector (such as a backbone N–H bond) is given by a simple geometric relationship that is dependent on the magnitude of the principal component of the alignment tensor D_a, the rhombicity of the tensor η, and two angles θ and ϕ describing the orientation of the vector relative to the *x*, *y*, and *z* axes of the alignment tensor (Figure I). RDCs are especially powerful for determining the relative orientation of two proteins within a complex as the two components share the same alignment tensor, and if the proteins can be treated as rigid bodies, only a small number of RDCs are required [43]. As a result it is possible to obtain an accurate structure of a protein–protein complex on the basis of only a few intermolecular NOEs to provide translational information, supplemented by RDCs for orientation.

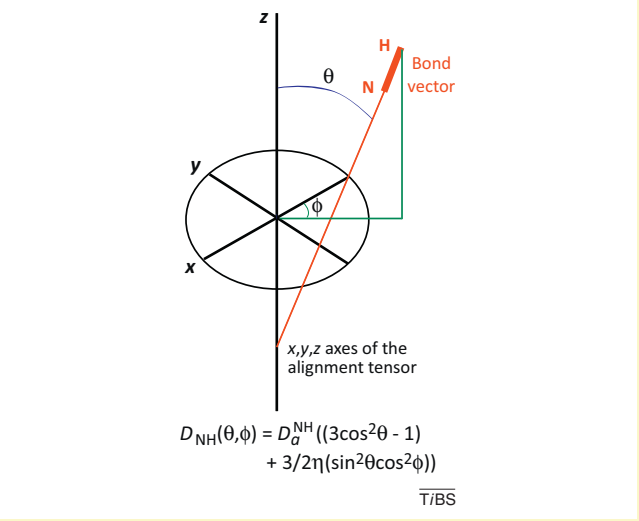

Figure I. Relationship between bond vector (N–H) orientation, the axes of the alignment tensor, and the corresponding RDC.

can make use of 3D ^{12}C-filtered/^{13}C-separated NOE experiments to observe specifically NOEs from protons attached to ^{13}C in the first protein to protons attached to ^{12}C in the second. Many other labeling combinations can also be used, including ^{13}C-labeling one protein and ^{15}N-labeling the second to observe NOEs between protons attached to ^{13}C in the first protein and protons attached to ^{15}N in the second. As the complexity and size of the complex increases, it is also useful to make use of residue-specific isotope labeling, especially of methyl bearing side chains.

In solving the structures of the IIA-HPr [45,47–49] and IIA–IIB [19,20,50,51] complexes, existing crystal structures of the individual domains were used where available and their accuracy verified by agreement of RDCs with the coordinates; structures involving IIB^{Glc}, IIB^{Mtl}, IIB^{Man}, and IIA^{Chb} made use of high-accuracy NMR structures solved on the basis of extensive NOE and RDC data; finally, in the case of IIB^{Chb}, the X-ray coordinates were used while giving the active site loop torsional degrees of freedom. Interestingly, the crystal structure of IIB^{Glc} in complex with the global repressor Mlc [52] was solved 5 years after the NMR structure of IIB^{Glc} complexed to IIA^{Glc} [19], and the backbone atomic rms difference between the IIB^{Glc} structures was only 0.37 Å, making IIB^{Glc} one of the most accurate *de novo* NMR structures determined to date, prior to the availability of an X-ray structure.

Solution structures of the PTS complexes – specific recognition of structurally diverse partners

The structures of all nine soluble complexes of the PTS are presented in Figure 1. HPr interacts with five different proteins (EIN, IIA^{Glc}, IIA^{Mtl}, IIA^{Man}, and IIA^{Chb}) that display no similarities with regard to primary, secondary, tertiary, or quaternary structure. The only apparent commonality is that the active site residue is a histidine, and in each case a pentacoordinate phosphoryl transition state can be modeled without necessitating any significant change in backbone coordinates. For the four IIA–IIB complexes, three involve phosphoryl transfer from a histidine on IIA to a cysteine on IIB. In the IIA^{Man}–IIB^{Man} complex, phosphoryl transfer occurs from a histidine to a histidine. As in the case of the complexes with HPr, the phosphoryl transition state can be modeled with no significant changes in backbone coordinates. Thus, phosphoryl transfer for all cytoplasmic complexes of the PTS can proceed with maximum energetic efficiency without incurring an energetic penalty from any significant conformational changes required for either partner protein.

Despite the apparent lack of similarity in the complexes at the level of the ribbon diagrams shown in Figure 1B, the interaction surfaces are actually similar despite the different underlying secondary and tertiary structural elements. This is apparent from the molecular surface representations of the interfaces shown in Figure 2. All the protein–protein interfaces are characterized by large buried accessible surface areas ranging from 1200 to 1800 Å^2, with approximately equal contributions from both partners. The interaction surfaces for HPr and Enzymes IIB are convex, whereas those of EIN and Enzymes IIA are concave, providing shape complementarity. In general, each interaction surface comprises a predominantly hydrophobic central region interspersed with scattered polar residues, and asymmetrically distributed charged residues at judicious locations along the outer edges of the interaction

Box 2. Simulating annealing

Simulating annealing is a heuristic global optimization method that is highly effective in circumventing local minima on the path to the global minimum of the target function being minimized. The underlying basis involves heating the system followed by slow cooling that has the effect of slowly decreasing the probability of accepting worse solutions, thereby permitting an extensive search for the optimal solution (i.e., the global minimum). There are several implementations of simulated annealing, including Monte Carlo methods and molecular dynamics. In the case of the complexes of the PTS, molecular-dynamics-based simulated annealing was used [44]. Several modalities can be used in combination, permitting parts of the system to be treated as rigid bodies while giving conformational degrees of freedom (either in torsion angle space or in Cartesian coordinate space) to other parts (such as interfacial side chains or linkers connecting two proteins). The target function that is minimized comprises terms for the experimental restraints (e.g., NOE-derived interproton distances, torsion angles, chemical shifts, RDCs, paramagnetic relaxation enhancement data, and X-ray scattering data), nonbonded contact terms to prevent atomic overlap, conformational database potentials to ensure that torsion angles lie in physically realistic regions of conformational space, and geometric restraints. In most instances only a single set of coordinates is refined against the experimental data. In some instances, however, especially when dealing with encounter complexes, an ensemble of structures is required to represent data. This necessitates the use of ensemble refinement where multiple copies of the coordinates are refined simultaneously.

surface. The active site residue is offset from the center of the binding site. Surface complementarity is largely provided by the hydrophobic residues, whereas electrostatic interactions serve to modulate affinity and direct the exact relative orientation of the partner proteins within a given complex. Sequences comparisons over several species indicate that although the absolute identity of the hydrophobic residues at the interface may vary, the network of intermolecular hydrophobic interactions is preserved and substitutions are in general compensatory, such that the packing density at the interface across different species remains largely unperturbed [19,42].

HPr uses essentially the same convex surface to interact with all its partners, and all charged residues on the interaction surface of HPr are positive (Figure 2A, top row). A key feature of the interactions of HPr with its partner proteins is redundancy of charged residues, such that the disposition of the complementary negatively charged residues on the partner proteins need not be identical. Thus, not all charged residues present at the protein–protein interface are involved in salt bridge interactions. In the same vein, each Enzyme IIA uses largely the same binding surface to interact with HPr and its IIB partner (compare the middle row of Figure 2A with the upper row of Figure 2B).

One might therefore ask why it is that the Enzymes IIB cannot bypass the corresponding Enzymes IIA and interact directly with EIN? The is because the binding surfaces on all the Enzymes IIB differ from that of HPr in one very significant way: although the majority of charged residues in the IIB binding site are positive, there are one or two negatively charged residues (Figure 2B, middle row) that complement positively charged residues on the corresponding IIA (Figure 2B, upper row), but would be repulsed by negatively charged residues on the surface of EIN (Figure 2A, upper row).

Another key feature of the binding surfaces that permits specific recognition of a wide variety of partners is side chain conformational plasticity, illustrated in Figure 3A for several side chain interactions between HPr and EIN or IIA^{Glc} [47]. For example, the side chain of Phe48 undergoes a conformational switch from one rotamer in the EIN–HPr complex to another in the IIA^{Glc}–HPr complexes, thereby permitting Phe48 to interact with hydrophobic components on the partner proteins, specifically the methyl groups of Leu79, Leu85 and Ile108 for EIN, and the backbone residues of a β-sheet for IIA^{Glc} (Figure 3A, left panel). Likewise, Arg17 of HPr interacts in one side conformation with Glu67 and Glu68 of EIN and in another conformation with Asp38 and Asp94 of IIA^{Glc} (Figure 3A, right panel)

The phosphoryl transition state intermediate

Phosphoryl transfer in the PTS complex occurs via in-line phosphoryl transfer in which the donor atom, the phosphorus, and the acceptor atom lie along a straight line [53]. Isotope labeling experiments have shown that odd and even numbers of phosphoryl transfer steps result in inversion and retention, respectively, of the configuration of the phosphorus [54,55], indicating that the transition state involves a pentacoordinate phosphoryl transition state in a trigonal bipyramidal geometry, with the donor and acceptor atoms in apical positions, and the oxygen atoms lying in the equatorial plane. The phosphoryl transition states can be modeled by introducing a phosphoryl group subject to restraints related to trigonal bipyramidal geometry at the phosphorus group. Phosphorylation occurs at the His(Nε2) atom for EIN and the four Enzymes IIA, at the His(Nδ1) atom for HPr and IIB^{Man}, and at the Sγ atom of cysteine for the remaining Enzymes IIB. The phosphoryl transition state can be formed without altering the position of the two partner proteins and with minimal changes in backbone coordinates immediately adjacent to the active site histidine or cysteine residues (Figure 2A,B, bottom row). The distances between the acceptor and donor atoms in the transition state can potentially range from the sum of the donor atom–phosphorus atom and phosphorus atom–acceptor atom bond lengths to the sum of the van der Waals radii of the donor, phosphorus (×2) and acceptor atoms, corresponding to fully associative and fully dissociative mechanisms, respectively. The N–P and S–P distances in the modeled transition states are consistent with substantial dissociative character, as predicted from a comparison of linear free energy relations for nonenzymatic and enzymatic phosphoryl transfer reactions [56]. Although the resolution of the structures of the complexes is limited, a fully associative mechanism would require substantial distortions and strain in the backbone adjacent to the donor and acceptor residues.

The phoshoryl transition states are shown in the lower rows of Figure 2A,B. The phosphoryl group and the active site histidines and/or cysteines lie on a bed of hydrophobic residues, and the phosphoryl group itself is stabilized by hydrogen bonding interactions involving polar (Thr, Ser, and His) or charged (Arg) residues. The number of hydrogen bonds to the phosphoryl group from each partner (both in the transition state and in models of the individual

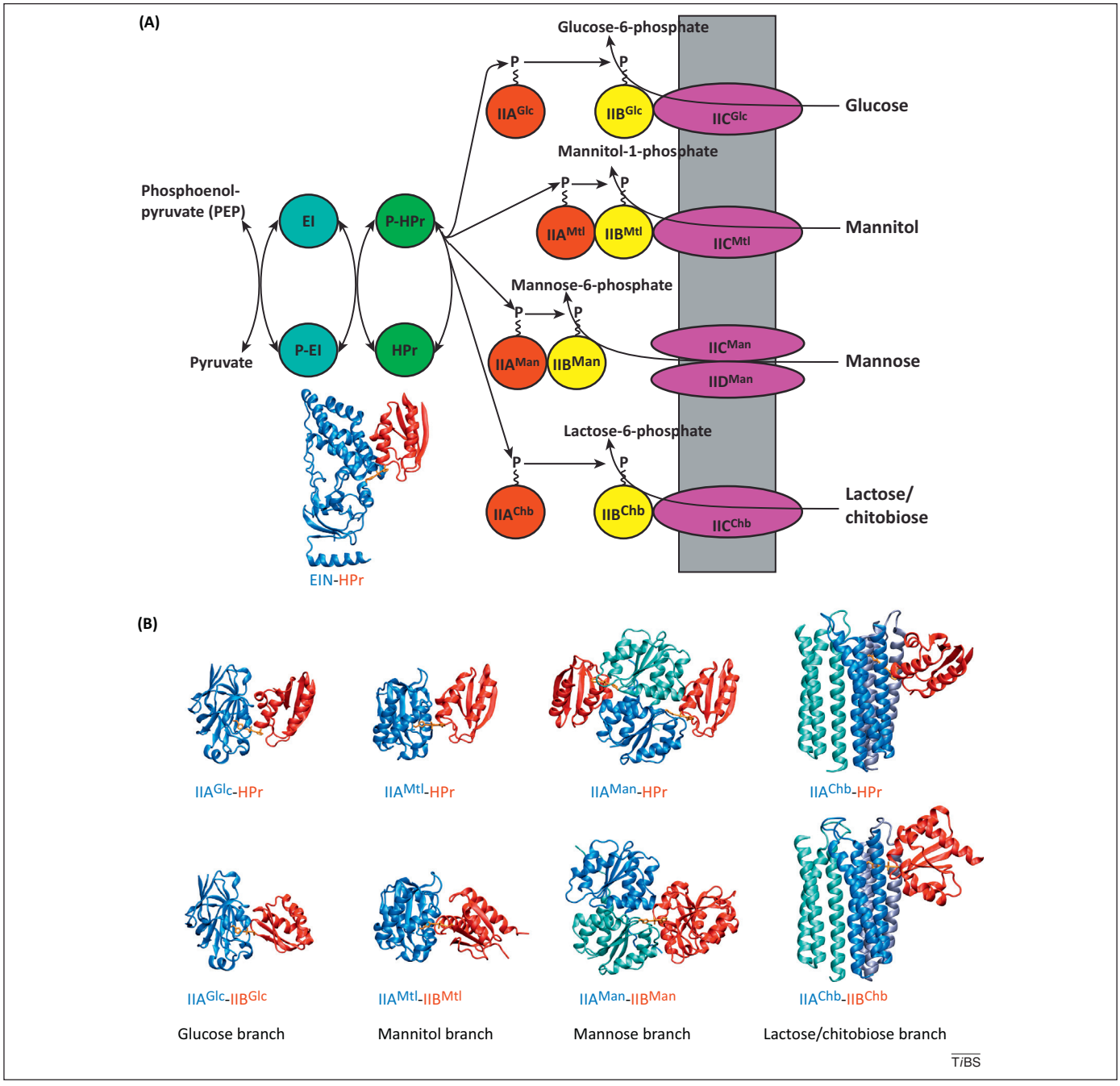

Figure 1. Summary of the PTS signal transduction pathway. **(A)** The first two steps are common to all branches of the pathway. Thereafter, the pathway splits into four sugar-specific classes: glucose, mannitol, mannose, and lactose/chitobiose. **(B)** Ribbon diagrams of the structures of the nine cytoplasmic complexes of the *Escherichia coli* PTS. EIN–HPr [42] (shown in A); IIA^{Glc}–HPr [47]; IIA^{Mtl}–HPr [45]; IIA^{Man}–HPr[48]; IIA^{Chb}–HPr [49]; IIA^{Glc}–IIB^{Glc} [19]; IIA^{Mtl}–IIB^{Mtl} [50]; IIA^{Man}–IIB^{Man} [20]; IIA^{Chb}–IIB^{Chb} [51]. Abbreviations: EIN, N-terminal domain of Enzyme I; HPr, histidine phosphocarrier protein; IIA, Enzyme II domain A; IIB, Enzyme II domain B; PTS, phosphotransferase system.

phosphorylated proteins), at least in the case of the glucose pathway where measurements of the various equilibria are available, correlates with the directionality of phosphoryl transfer. Thus, the phosphoryl transfer from EIN to HPr and from IIA^{Glc} to IIB^{Glc} are favored by factors of ~10 and ~3, respectively, over the reverse transfers, whereas the phosphoryl transfers from HPr to IIA^{Glc} and from IIA^{Glc} to HPr are equally favorable [57], consistent with the larger number of hydrogen bonds stabilizing the phosphoryl group originating from HPr than EIN and from IIB^{Glc} than IIA^{Glc}, whereas the same number of hydrogen bonds stabilize the phosphoryl group in HPr and IIA^{Glc}.

Impact of linkers connecting PTS domains on the efficiency of phosphoryl transfer

Many of the domains of Enzymes II are connected by long flexible linkers. For example, the A, B, and transmembrane C domains of Enzyme $IIABC^{Mtl}$ and the A and B domains of Enzyme $IIAB^{Man}$ are expressed as single proteins, as are the IIB^{Glc} and transmembrane IIC^{Glc} domains of $IIBC^{Glc}$ [3]. In addition, many of the PTS complexes have K_d values in the high micromolar to millimolar range [20,45,48–51]. The K_d for the interaction of the isolated IIA^{Mtl} and IIB^{Mtl} domains is 3–4 mM [50], whereas that of the isolated IIA^{Man} and IIB^{Man} domains is ~0.5 mM [20].

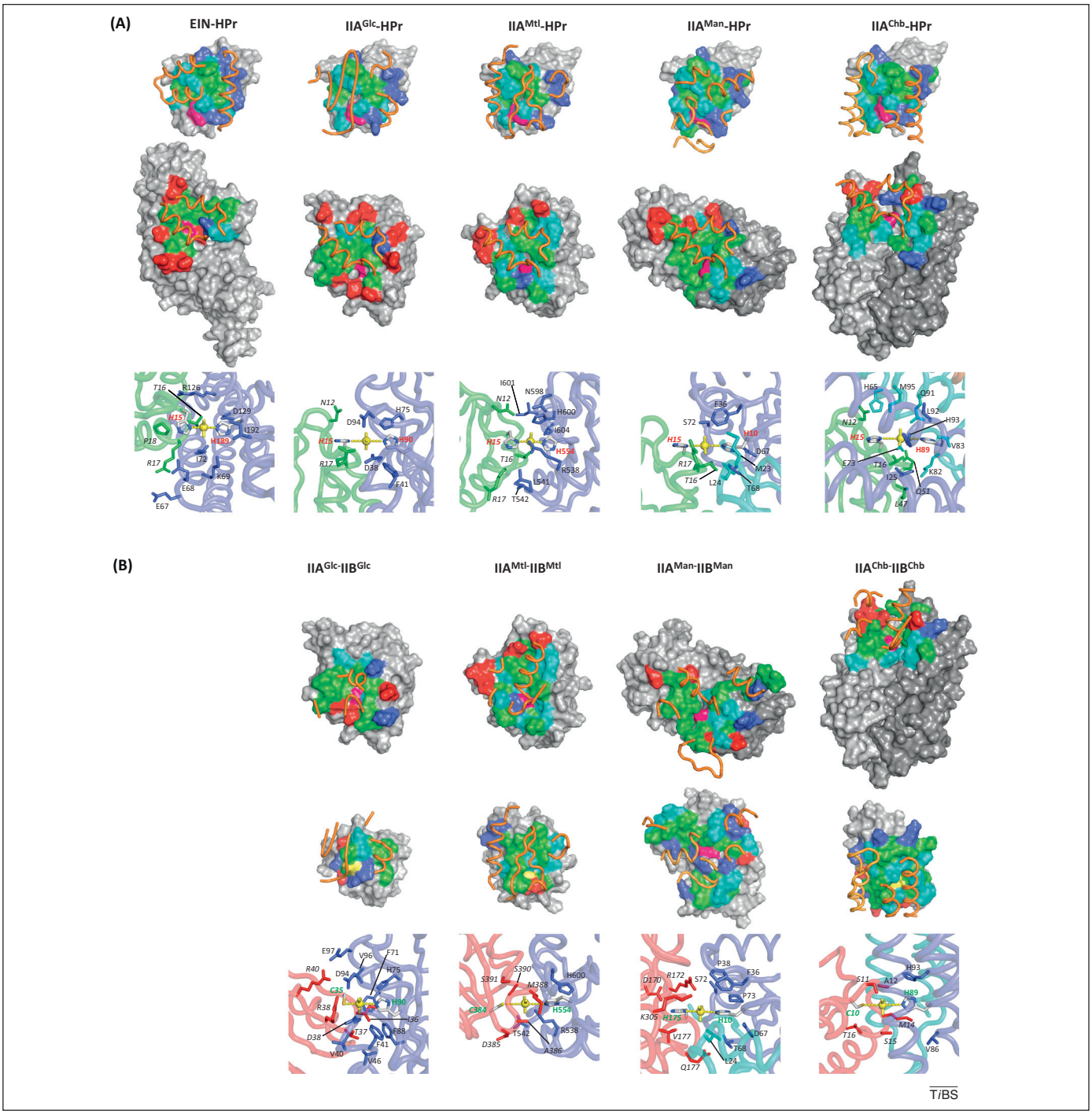

Figure 2. Summary of interaction surfaces for the cytoplasmic complexes of the PTS. Complexes of EIN and the four classes of Enzymes IIA with HPr and of the four classes of Enzymes IIA with their respective Enzyme IIB counterparts. **(A)** Top row, interaction surfaces on HPr; middle row, interaction surfaces on EIN and Enzymes IIA; bottom row, close up of the phoshoryl transition states. **(B)** Top row, interaction surfaces on Enzymes IIA; middle row, interaction surfaces on Enzymes IIB; bottom row, close up of the phoshoryl transition states. For both panels, residues on the interaction surfaces (top and middle rows) are color-coded as hydrophobic (green), hydrophilic (cyan), positively charged (blue), negatively charged (red), active site histidine (purple), and active site cysteine (yellow). Also shown in the top and middle rows are the relevant portions of the backbone of the interacting partner displayed as gold tubes. In the bottom row of panel A, HPr is displayed in green, EIN and Enzymes IIA in blue, and the pentacoordinate phosphoryl group in yellow; residues labels for HPr are in italics. In the bottom row of panel B, Enzymes IIB are displayed in red, Enzymes IIA in blue, and the pentacoordinate phosphoryl group in yellow; residues labels for Enzymes IIB are in italics. EIN–HPr [42]; IIA^{Glc}–HPr [47]; IIA^{Mtl}–HPr [45]; IIA^{Man}–HPr [48]; IIA^{Chb}–HPr [49]; IIA^{Glc}–IIB^{Glc} [19]; IIA^{Mtl}–IIB^{Mtl} [50]; IIA^{Man}–IIB^{Man} [20]; IIA^{Chb}–IIB^{Chb} [51]. Abbreviations: EIN, N-terminal domain of Enzyme I; HPr, histidine phosphocarrier protein; IIA, Enzyme II domain A; IIB, Enzyme II domain B; PTS, phosphotransferase system.

Tethering two domains increases their effective local concentration, thereby increasing the probability of complex formation. The A and B domains of II^{Mtl} are connected by a 21-residue flexible linker, from which one can calculate, using well-established polymer chain theory, that the effective local concentration of the A and B domains is ~4 mM [50]. This value is consistent with ^{15}N relaxation dispersion measurements on IIAB^{Mtl} that yield a population of ~50% for the associated state with a unimolecular association rate constant of ~20 000 s^{-1} for the interaction

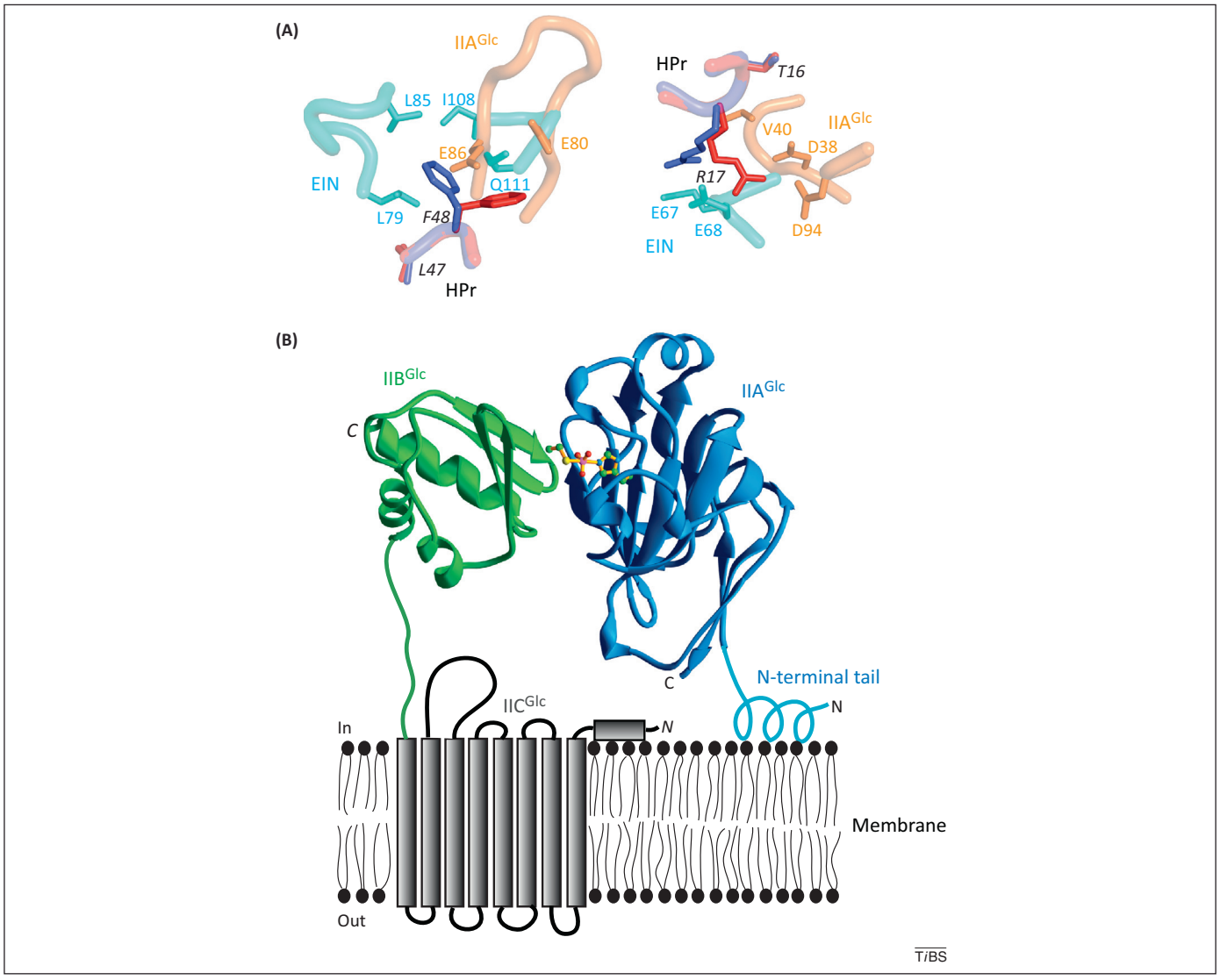

Figure 3. Role of conformational side chain plasticity and membrane-anchoring tails in protein complexes of the PTS. **(A)** Conformational side chain plasticity illustrated by complexes of HPr with EIN and IIA^{Glc}. EIN is shown in cyan, IIA^{Glc} in orange, HPr in the EIN–HPr complex in blue, and HPr in the IIA^{Glc}–HPr complex in red. Residues of HPr are labeled in italics. Alternate conformations for *Phe48* and *Arg17* of HPr are illustrated in the left and right panels, respectively. Adapted from [47]. **(B)** Role of the N-terminal tail of IIA^{Glc} in facilitating phosphotransfer to $IIBC^{Glc}$. IIA^{Glc} is shown in blue and residues 2–10 adopt a helical conformation upon interaction with the lipid bilayer of the bacterial cell membrane, thereby stabilizing the IIA^{Glc}–$IIBC^{Glc}$ complex by partially anchoring IIA^{Glc} to the lipid membrane. IIB^{Glc} is shown in green, and a cartoon of the transmembrane IIC^{Glc} domain which includes eight transmembrane helices is shown in gray. Adapted from [19]. Abbreviations: EIN, N-terminal domain of Enzyme I; HPr, histidine phosphocarrier protein; IIA, Enzyme II domain A; IIB, Enzyme II domain B; PTS, phosphotransferase system.

of the tethered A and B domains [58]. The latter corresponds to an apparent bimolecular association rate constant of $5\times10^6\ M^{-1}\ s^{-1}$ [58] which is within the range typically observed for specific protein–protein interactions (0.5×10^6–$5\times10^6\ M^{-1}\ s^{-1}$) and in excellent agreement with the predicted value of $2\times10^6\ M^{-1}\ s^{-1}$ for a purely diffusive process obtained from Brownian dynamics simulations [59]. Thus, the linker serves to tune the system optimally to achieve reasonable high occupancy coupled with rapid association and dissociation ($\sim$20 000 s^{-1} in both directions) to carry out efficiently three sequential phosphoryl transfer steps from HPr to IIA^{Mtl}, from IIA^{Mtl} to IIB^{Mtl}, and finally from IIB^{Mtl} onto the incoming sugar bound to the cytosolic side of IIC^{Mtl}. The phosphoryl transfer rate between the A and B domains of IIA^{Mtl} determined from NMR lineshape analysis is $\sim$500 s^{-1} in both directions [58]. This value is $\sim$40-fold lower than the rate constants for intramolecular domain–domain association and dissociation, therefore, one can calculate that $\sim$80 association/dissociation events take place for every phosphoryl transfer reaction. Thus, the rate-limiting step for phosphoryl transfer between the A and B domains of $IIAB^{Mtl}$ is governed by the chemistry of the phosphoryl transfer reaction itself rather than the rate of association to form the specific complex or the rate of dissociation to permit the next phosphoryl transfer reaction in the pathway to take place.

The glucose Enzymes II exhibit a variant of this phenomenon. Although the B and C domains are tethered by a $\sim$75-residue linker, the A domain is expressed as a separate protein. The first 18 residues of IIA^{Glc} are disordered in solution and although the presence or absence of the N-terminal tail has no effect on phosphoryl transfer between HPr and IIA^{Glc}, the presence of the N-terminal tail is critical for efficient phosphoryl transfer to IIB^{Glc} *in vivo*

[60,61]. It turns out that residues 2–10 of the N-terminal tail of IIA^{Glc} associate with *Escherichia coli* membranes to form an amphiphatic helix [62], thereby bringing IIA^{Glc} in close proximity to IIB^{Glc} and stabilizing the IIA^{Glc}–IIB^{Glc} interaction by effectively increasing the local concentration of IIA^{Glc} and $IIBC^{Glc}$ (Figure 3B).

Solution structure of intact EI and its complex with HPr – approaches to solving structures of larger (>100 kDa) complexes in solution

The N-terminal domain (EIN) of EI can transfer a phosphoryl group to and accept a phosphoryl group from HPr but cannot be autophosphorylated by PEP [63–66]. Autophosphorylation of EI requires the presence of the C-terminal dimerization domain EIC. Intact EI is a 128-kDa dimer and therefore large by NMR standards. The probability of successfully solving a structure of this size using conventional NMR methodology is small, and even if it could be done, the coordinate accuracy would be low. To solve the solution structure efficiently and accurately of such a system therefore requires the development of hybrid methodology that makes use of prior available structural information combined with limited solution RDC and small (SAXS) and wide (WAXS) angle X-ray scattering [40].

The crystal structure of a trapped phosphorylated intermediate of intact *E. coli* (Figure 4A, middle panel, and Figure 4B, left panel) has been solved by crystallizing EI from a solution containing PEP and Mg^{2+} and then quenching the autophosphorylation reaction using the inhibitor oxalate [33]. A comparison of the structure of the EIN domain in the EI phosphorylated intermediate with that of the isolated EIN domain, both free (X-ray [30] and NMR [39]) and complexed to HPr [42], reveals major conformational changes in the disposition of the two subdomains, α and α/β, of EIN (Figure 4A). The EIN^{α} subdomain provides the interaction surface for HPr, whereas the $EIN^{\alpha/\beta}$ subdomain contains the active site histidine, His189 [42]. The position of the active site histidines of HPr (His15) and EIN (His189) in the EIN–HPr complex allows for in-line phosphoryl transfer between EIN and HPr without requiring any substantial conformational changes (Figures 2A and 4A, left panel) [42]. In the phosphorylated EI intermediate [33], the EIN^{α} subdomain undergoes a reorientation of ~70° relative to the $EIN^{\alpha/\beta}$ subdomain, such that the Cα–Cα distance between the active site histidines of HPr and EIN would be increased from ~12 Å in the EIN–HPr complex to ~30 Å (Figure 4A, middle panel); a distance too large to permit phosphoryl transfer from EIN to HPr. However, the active site His189 in the $EIN^{\alpha/\beta}$ subdomain of the phosphorylated EI intermediate is optimally positioned for phosphoryl transfer from PEP bound to the EIC domain to His189 (Figure 4A, left panel) [33]. If the orientation of the $EIN^{\alpha/\beta}$ subdomain relative to the EIC dimer in the crystal structure of the phosphorylated intermediate were preserved, the EIN^{α} subdomain would interpenetrate the EIC domain in the configuration found in the isolated EIN domain (Figure 4A). Thus, the transition from free EI to phosphorylated EI must be accompanied by two major rigid body conformational rearrangements involving reorientation of $EIN^{\alpha/\beta}$ relative to EIC and of EIN^{α} relative to $EIN^{\alpha/\beta}$.

RDCs measured on the EIN domain of intact EI (both free and complexed to HPr) are in excellent agreement with the orientation of the EIN^{α} and $EIN^{\alpha/\beta}$ subdomains in the isolated EIN domain, but are inconsistent with that in the crystal structure of the EI phosphorylated intermediate. Thus, one can conclude unambiguously that the relative orientation of the EIN^{α} and $EIN^{\alpha/\beta}$ subdomains in free and HPr-bound full-length EI remains unchanged relative to that in the isolated EIN domain [40].

The hybrid approach used to solve the structure of free EI and the EI–HPr complex made combined use of RDCs and SAXS/WAXS. The RDCs restrain the relative orientations of the EIN^{α} and $EIN^{\alpha/\beta}$ subdomains within each subunit and of the two symmetry-related EIN domains in the dimer. The structure of the EIC domain dimer is the same in several EI and isolated EIC structures [33–35,67,68]; therefore the orientation of the symmetry-related EIN domains relative to the EIC dimer can be determined from RDCs located only in the EIN domain, as one of the principal axes of the alignment tensor must coincide with the C_2 symmetry axis of the dimer (since the RDCs for the two identical subunits are the same). RDCs alone are not sufficient to determine a unique structure, owing to the existence of several equivalent solutions arising from the intrinsic equivalence of 180° rotations about the axes of the RDC alignment tensor. However, when the RDCs are combined with stereochemical and covalent geometry restraints within the linker connecting the EIN and EIC domains together with shape and translational information contained within the SAXS/WAXS profiles, only a single solution emerges from RDC and SAXS/WAXS-driven simulated annealing calculations, in which the domains are treated as rigid bodies and only the linker (residues 255–261) is allowed to vary in conformation [40,41].

The RDCs and SAXS/WAXS profiles [40] do not agree with the crystal structures of phosphorylated *E. coli* EI (Figure 4B, left panel) [33] or free *Staphylococcus aureus* [35] and *Staphylococcus carnosus* [34] EI. The χ^2 for the fits to the SAXS/WAXS data (from scattering vector values of q = 0.014–0.44 $Å^{-1}$) are 128, 56, and 30 for the three crystal structures, respectively. The same is true of small angle neutron scattering (SANS) with χ^2 values of 62, 34, and 30, respectively. Moreover, the calculated Svdeberg sedimentation coefficient for phosphorylated EI (S = 6.74) and free *S. aureus* EI (S = 6.45) are significantly larger than the experimental value (S = 5.68) determined by sedimentation velocity, indicating that the structures are too compact, whereas that for *S. carnosus* EI (5.55) is too small [40], reflecting an overly expanded structure. In addition, the structure of the EIN domain in the *S. carnosus* crystal structure is partially disordered.

The solution structures of *E. coli* free EI and EI complexed to HPr determined by conjoined rigid body/torsion angle/Cartesian simulated annealing driven by RDCs and SAXS/WAXS are shown in Figure 4B [40]. Both structures are independently validated by agreement to both WAXS at high q (0.44–0.8 $Å^{-1}$) and SANS. The latter provides an independent validation tool for the EI–HPr complex as contrast-matching was used to render the HPr component invisible (by using a complex of deuterated EI and protonated HPr in 40.4% D_2O).

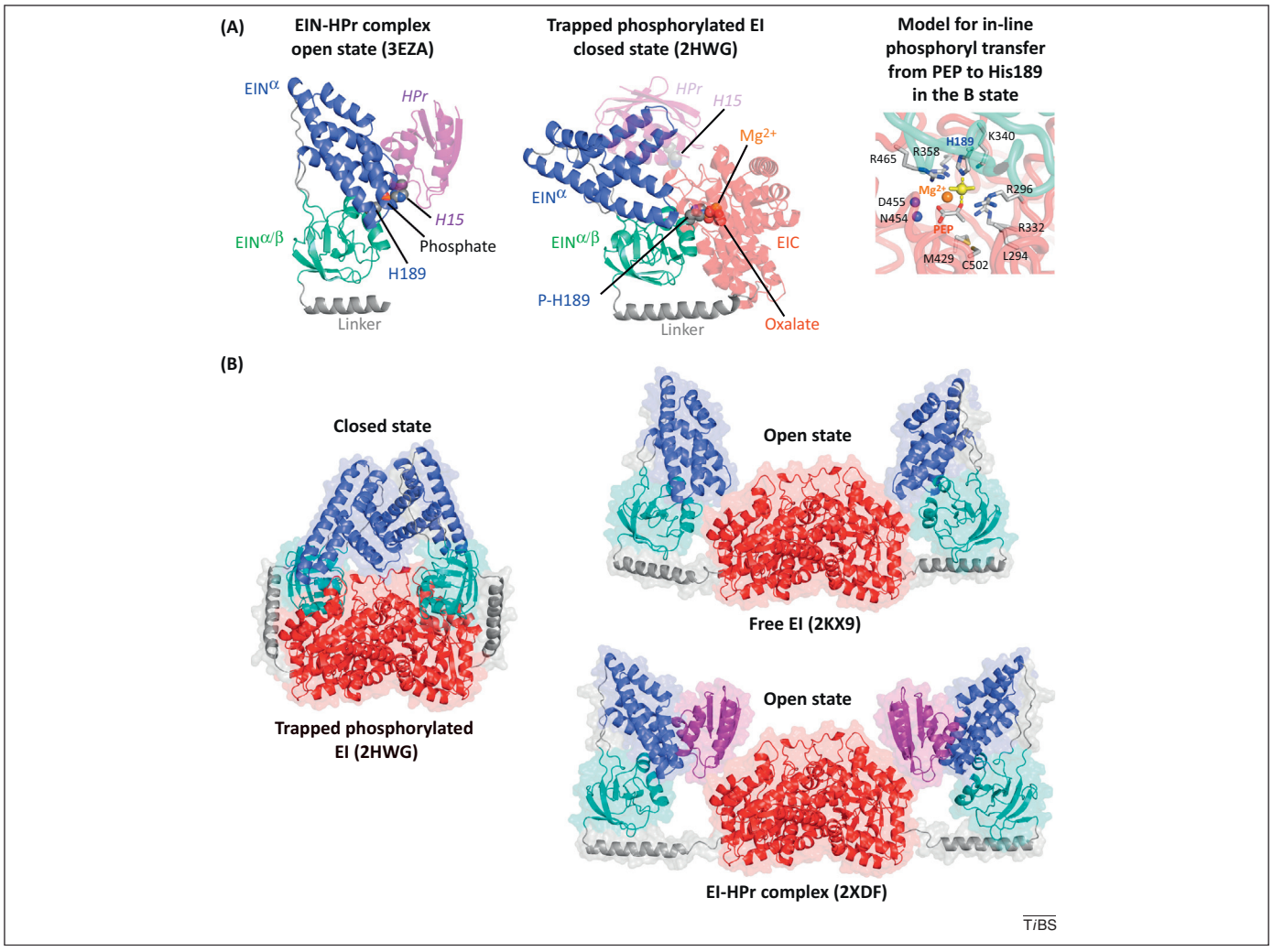

Figure 4. Comparison of open and closed states of EI. **(A)** The open state is found in the isolated EIN domain (left panel) and in intact EI, both free and in complex with HPr [30,39–42]; the closed state (middle panel) is found in the crystal structure of the trapped phosphorylated intermediate of EI [33]. The $EIN^{\alpha/\beta}$ subdomain (cyan) is shown in the same orientation in both panels. Only a single subunit of phosphorylated EI is shown. The color coding is as follows: EIN^{α}, blue; $EIN^{\alpha/\beta}$, cyan; EIC, red; linker connecting $EIN^{\alpha/\beta}$ to EIC, brown; HPr, purple. HPr bound to the EIN^{α} subdomain of phosphorylated EI (closed state) in the same orientation as in the EIN–HPr complex (open state) is shown in the middle panel as a transparent purple ribbon to illustrate that the HPr binding site is available in the closed state and there are no clashes between HPr and EIC in this conformation, but that the distance between *His15* of HPr and His189 of EIN^{α} is much too large (~30 Å) to allow phosphoryl transfer from EIN to HPr to take place in the closed state. The right panel shows a model of in-line phosphoryl transfer from PEP to His189 in the closed state. **(B)** Comparison of the crystal structure of the trapped phosphorylated intermediate of the EI dimer (closed state) with the solution structures of the free EI dimer and the dimeric EI–HPr complex (open state) determined from combined use of NMR residual dipolar couplings and solution X-ray scattering (SAXS/WAXS). The color coding is the same as in (A). Abbreviations: EIN, N-terminal domain of Enzyme I; HPr, histidine phosphocarrier protein; IIA, Enzyme II domain A; IIB, Enzyme II domain B; PTS, phosphotransferase system.

The relative orientation of EIN relative to EIC in free EI and the EI–HPr complex are not identical (Figure 4B, right panel). For free EI, the EIN domain makes extensive contacts (~300 $Å^2$ of buried accessible surface area) with the EIC domain, with several complementary charge–charge interactions. In this configuration, HPr bound to the EIN^{α} subdomain would partially overlap with the EIC domain. Binding of HPr to the EIN^{α} subdomain is accompanied by additional movement of the EIN domain away from the EIC domain to make room for HPr, such that HPr is sandwiched between the EIN and EIC domains. There are a small number of contacts between HPr and EIC involving several complementary electrostatic interactions with a buried accessible surface area of ~100 $Å^2$. The conformational transition of the EIN domain from the free EI configuration to that of the EI–HPr configuration is achieved by only minor changes in backbone torsion angles within the linker connecting the $EIN^{\alpha/\beta}$ subdomain to the EIC domain.

Figure 5 depicts the postulated catalytic cycle for EI [40]. The change in configuration of the EIN domain from that of the phosphorylated EI intermediate to that of free EI and the EI–HPr complex must involve two sequential or concerted conformational transitions. First, a ~70° reorientation of $EIN^{\alpha/\beta}$ relative to EIC, accompanied by a ~34 Å rms displacement of the $EIN^{\alpha/\beta}$ subdomain. Second, a ~70° reorientation of EIN^{α} relative to $EIN^{\alpha/\beta}$ through backbone torsion angle changes within the two linkers joining the EIN^{α} to $EIN^{\alpha/\beta}$ subdomains. The latter cannot occur first because EIN^{α} would clash with EIC in the absence of any accompanying reorientation of $EIN^{\alpha/\beta}$.

Although the SAXS/WAXS, SANS and RDC data for EI and the EI–HPr complex can be satisfied by a single structure, it is likely that interdomain motions and sparsely

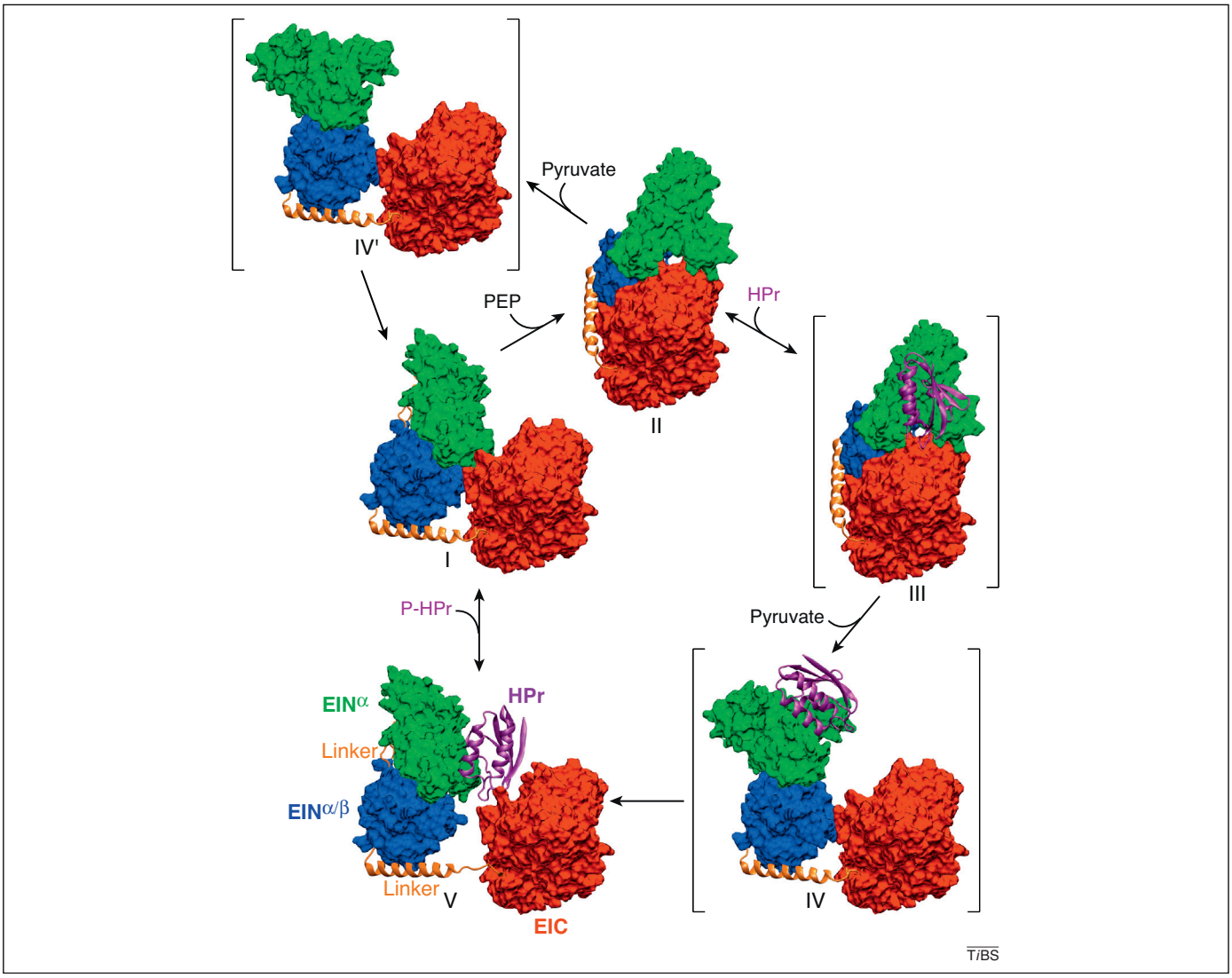

Figure 5. Catalytic cycle of EI. Only a single subunit is displayed for clarity with the molecular surfaces of the EIN^{α} and $EIN^{\alpha/\beta}$ subdomains of EIN in green and blue, respectively, the molecular surface of EIC domain in red, the linker connecting $EIN^{\alpha/\beta}$ to EIC in a gold ribbon, and HPr in a purple ribbon. Structures I and V correspond to free EI and the EI–HPr complex (open state) solved by NMR and SAXS/WAXS, structure II to the crystal structure of the trapped phosphorylated intermediate (closed state), and structures III, IV and IV′ (shown in brackets) to postulated intermediates. Structure III corresponds to the binding of HPr to the trapped phosphorylated intermediate; structures IV and IV′ correspond to structures in which the orientation of the $EIN^{\alpha/\beta}$ subdomain relative to EIC is the same as that in free EI (I) or the EI–HPr complex (V), whereas the orientation of the EIN^{α} subdomain relative to $EIN^{\alpha/\beta}$ is the same as that in the trapped phosphorylated intermediate (II). The EIC domain (red) is displayed in the same orientation for all structures. Adapted from [40]. Abbreviations: EIN, N-terminal domain of Enzyme I; HPr, histidine phosphocarrier protein; IIA, Enzyme II domain A; IIB, Enzyme II domain B; PTS, phosphotransferase system; SAXS, small angle X-ray scattering; WAXS, wide angle X-ray scattering.

populated states are present. However, because the RDC and X-ray scattering data are sensitive to different types of motion, the former being dependent on orientation and the latter on molecular size and shape, one can be confident that the calculated structures are representative of the predominant average structure in solution.

Interplay between conformational dynamics and dimerization of the EIC domain

Binding of PEP and Mg^{2+} to EI results in a ~30-fold decrease in the equilibrium dissociation constant (K_{dimer}) for the dimer [69,70]. The decrease in K_{dimer} upon ligand binding is thought to play an important role in regulating the PTS because only intact dimeric EI can be autophosphorylated by PEP [70]. Binding of PEP to the dimeric isolated EIC domain results in large $^{1}H_N/^{15}N$ chemical shift perturbations around the PEP binding site and in the adjacent β3α3 turn located at the dimer interface [71]. Examination of EIC in various crystal structures [33–35,67,68] suggests that the β3α3 turn exists in open and closed conformations, with the latter corresponding to the conformation in the phosphorylated EI intermediate (Figure 6). ^{15}N relaxation dispersion measurements reveal the existence of a dynamic equilibrium between major (97%) and minor (3%) species with an overall exchange rate of ~1550 s^{-1} [71]. The backbone ^{15}N chemical shift differences between the major and minor species in free EIC determined from the relaxation dispersion data correspond with the chemical shift differences observed upon addition of PEP [71]. Thus, it is likely that binding of PEP occurs via conformational selection of a low-population state corresponding to the closed state of the β3α3 turn.

Encounter complexes in the PTS

Specific protein–protein recognition generally proceeds via a two-step process involving the initial formation of an

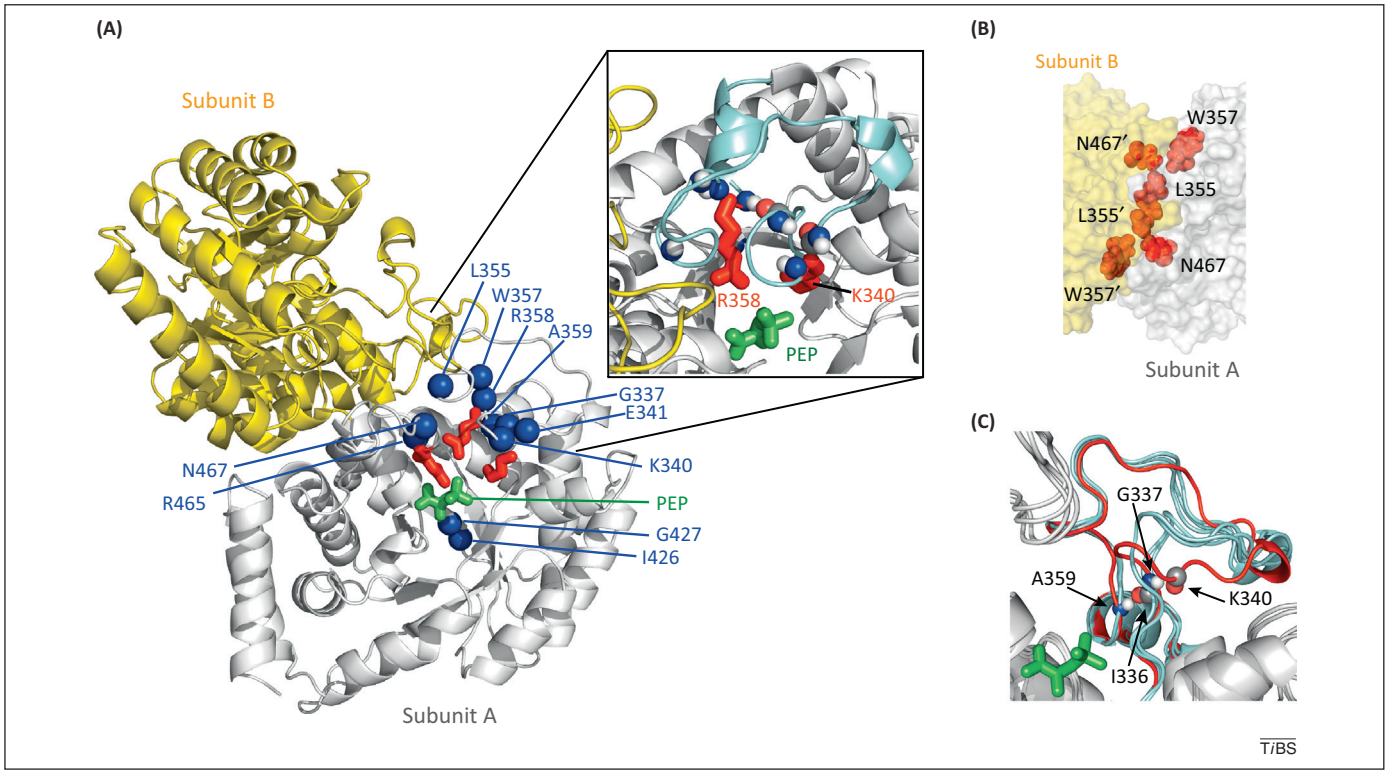

Figure 6. Structure and dynamics of the isolated EIC dimer. **(A)** Structural model of the *Escherichia coli* EIC–PEP complex derived from the crystal structures of the *T. tengcongensis* EIC–PEP complex [68] and the *E. coli* phosphorylated EI intermediate [33]. One subunit is in gray, the other in yellow. PEP is in green; the side chains of Lys340, Arg358, and Arg 465 in red; and backbone nitrogen atoms exhibiting significant relaxation dispersion, characteristic of motion on the submillisecond to millisecond time scale, in blue. The inset shows a close-up of the β3α3 turn. **(B)** Close-up view of the EIC dimer interface. **(C)** Superposition of the crystal structures of EIC [33–35,67,68], illustrating the conformational variability of the β3α3 turn, with the closed conformation of the β3α3 turn seen in the crystal structure of the trapped phosphorylated EI intermediate in red. **(D)** The overall exchange rate between major (97%) and minor (3%) species determined by ^{15}N-NMR relaxation dispersion spectroscopy is ~1550 s^{-1}. The ^{15}N chemical shift differences between the major and minor species determined from relaxation dispersion on free EIC correspond closely to the differences in chemical shifts between free EIC and EIC complexed to PEP, strongly suggesting that the minor species represents the closed conformation of the β3α3 turn. Adapted from [71]. Abbreviations: EI, Enzyme I; EIC, Enzyme I C-terminal dimerization domain; PEP, phosphoenolpyruvate.

ensemble of short-lived encounter complexes via diffusion-controlled intermolecular collisions, followed by translations and rotations of the two partner proteins down a 2D funnel-like energy landscape, resulting in the formation of a well-defined specific complex stabilized by a complementary set of electrostatic and van der Waals interactions [72,73]. Encounter complexes are thought to play an important functional role in fine-tuning reaction fluxes inside the cell [74] by enhancing association on-rates through an increase in the interaction cross-section and a reduction in the conformational search space on the path to the specific complex [75–78]. Encounter complexes are generally extremely difficult to study experimentally because they are short-lived, highly transient, and sparsely populated, and therefore invisible to conventional structural and biophysical methods.

Transient, sparsely populated states, however, can be studied by NMR using paramagnetic relaxation enhancement (PRE) (Box 3). A comparison of the experimental PRE profiles for the EIN–HPr complex with those calculated from the structure of the specific EIN–HPr complex is shown in Figure 7A [79]. The paramagnetic tag (EDTA-Mn^{2+}) that gives rise to the PRE is covalently attached to three sites (E5C, E25C, and E32C) on HPr (at natural isotopic abundance) using surface engineered cysteines, whereas EIN is uniformly labeled with ^{15}N. This isotopic labeling scheme permits one to detect specifically intermolecular PRE effects originating from the paramagnetic label attached to HPr on the backbone amide resonances of EIN. It can be seen that although there are features of the experimental intermolecular PRE profiles (black circles) that match the calculated profiles for the specific complex, there are regions where the observed intermolecular PREs (purple circles) are larger than the calculated values. Thus, there are regions on EIN that spend a small proportion of time closer to the paramagnetic tags on HPr than in the specific complex. Similar observations have been made for complexes of HPr with IIA^{Mtl} and IIA^{Man} [80].

The discrepancies between observed and calculated intermolecular PREs can be fully accounted for by the presence of a small population (5–10%) of transient encounter complexes whose distribution can be calculated using PRE-driven rigid body ensemble simulated annealing [80] (Box 2). The calculated distribution of HPr on the surface of EIN is largely correlated with surface electrostatics, which has been confirmed experimentally by the observation that the intermolecular PREs arising from the encounter complexes are significantly more sensitive to ionic strength than those from the specific complex [81].

Further analysis of the intermolecular PRE intensities as a function of added paramagnetically labeled HPr has yielded further insights into the nature of the encounter complexes [79]. The PREs attributable to the specific

Box 3. PRE and the detection of sparsely populated states

PRE is an NMR technique that involves covalently attaching a paramagnetic tag (such as a nitroxide or EDTA-Mn^{2+}) to an engineered surface exposed cysteine residue [80,99,100]. The PRE effect (measured by the difference in ^1H transverse relaxation rates between samples with and without the paramagnetic tag) is proportional to the $<r^{-6}>$ separation between the paramagnetic tag and the protons of interest. (^1H transverse relaxation rates reflect the linewidths of the ^1H resonances in the NMR spectrum, the larger the ^1H transverse relaxation rate, the broader the resonances). The magnetic moment of an unpaired electron is large, and therefore, the PRE at short distances is correspondingly large. For example, for a 20–30-kDa molecule, the transverse PRE rate (Γ_2) for a 30-Å distance would be ~2 s^{-1}, whereas that for an 8-Å distance would be ~6000 s^{-1}. In a system comprising two species, one populated at 99% with a distance of 30 Å, the other at 1% with a distance of 8 Å, that exchange fast on the PRE time scale (defined as an exchange rate larger than the difference in PRE rates for the two species), the PREs observed on the spectrum of the major species will be a population weighted average of the PRE rates for the major and minor species; in this particular example, the PRE rate measured on the spectrum of the major species would therefore be around 50–60 s^{-1}. As a result, the imprint of the invisible minor species will be reflected in the PRE profiles measured on the spectrum of the major species, providing there are paramagnetic tag-proton distances that are shorter in the minor species than the major one.

complex titrate as a simple one-site binding isotherm with a K_d of ~7 μM, in agreement with the K_d determined by isothermal titration calorimetry. The PREs arising from the encounter complexes, however, titrate as three classes (Figure 7B). Class I PREs display the same titration behavior as the intermolecular PREs arising from the specific complex. Thus, these intermolecular PREs arise from encounter complexes that are exclusive with the specific complex (i.e., the binding sites must overlap such that the specific complex and the class I encounter complexes cannot occur together). Class II PREs follow the concentration of free HPr, and therefore arise from encounter complexes that are nonexclusive with the specific complex (i.e., class II encounter complexes coexist with the specific complex). Finally, class III PREs exhibit a mixture of class I and II behavior. When the three classes of encounter complex PREs are mapped onto the surface of EIN, it is clear that class I PREs report on encounter complexes interactions near the active site of EIN that are occluded by the specific complex (Figure 7C). The class II PREs report on ternary $HPr_{nonspecific}$/EIN/HPr complexes that predominate when the active site is occupied by the specific complex (Figure 7C). These finding can be summarized by the equilibrium binding model shown in Figure 7D.

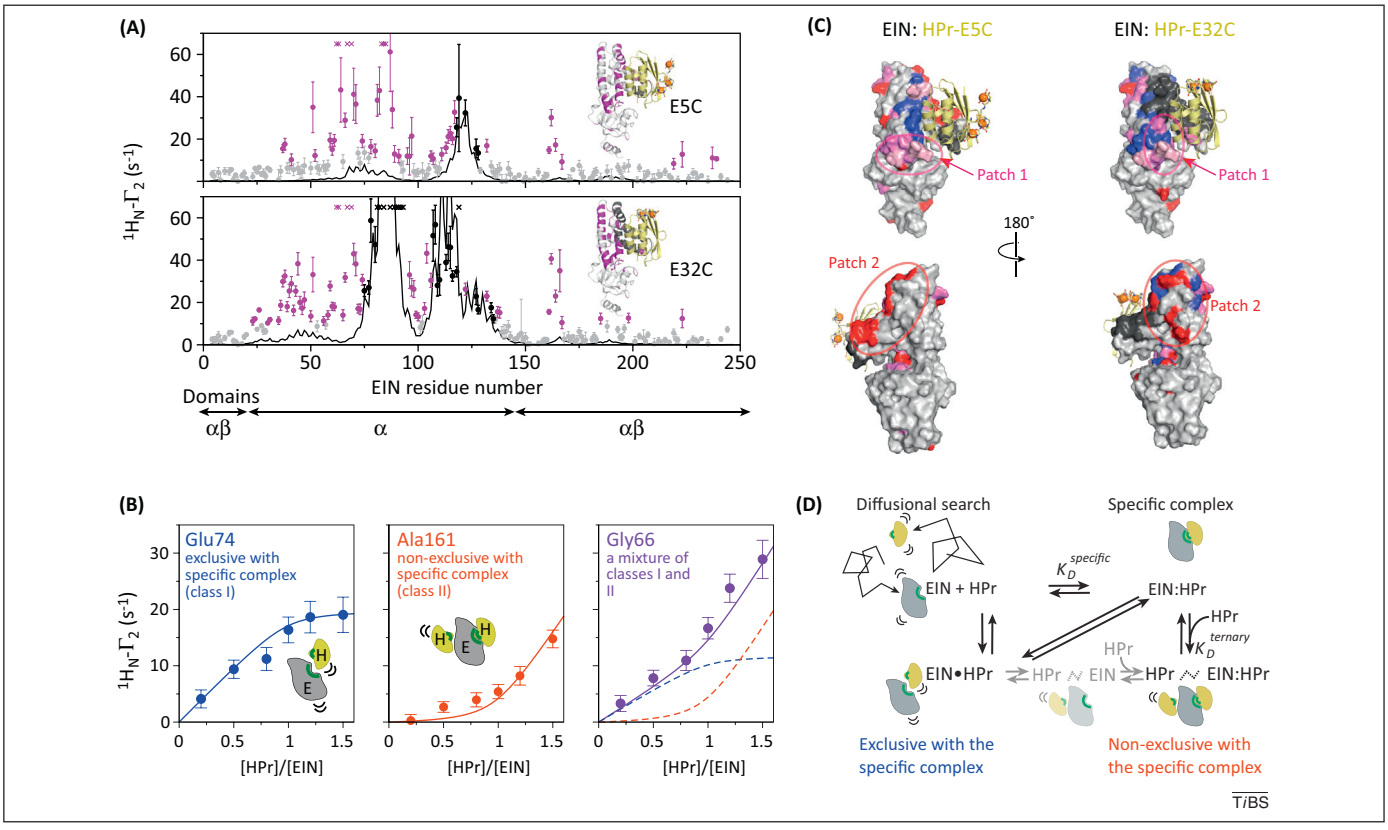

Figure 7. Characterization of transient sparsely populated encounter complexes for the interaction of EIN and HPr. **(A)** Comparison of experimental backbone amide intermolecular PREs (^1H_N-Γ_2) (circles) observed on ^{15}N-labeled EIN and arising from covalently attached paramagnetic tags (EDTA-Mn^{2+}) located at two positions on HPr (E5C and E32C) with the PRE profiles calculated from the structure of the specific complex (black line). Black and purple circles indicate PREs attributable to the specific complex and to an ensemble of encounter complexes, respectively. **(B)** Intermolecular PREs as a function of added paramagnetically-labeled HPr(E5C) illustrating three types of titration behavior. **(C)** Mapping of intermolecular PREs attributable to the specific complex (black) and to the encounter complexes (class I, blue; class II, red; mixture of classes I and II, purple; and encounter complex PREs that are too large to measure accurately, pink). **(D)** Equilibrium binding model for the EIN/HPr association pathway. Adapted from [79]. Abbreviations: EIN, N-terminal domain of Enzyme I; HPr, histidine phosphocarrier protein; PRE, paramagnetic relaxation enhancement.

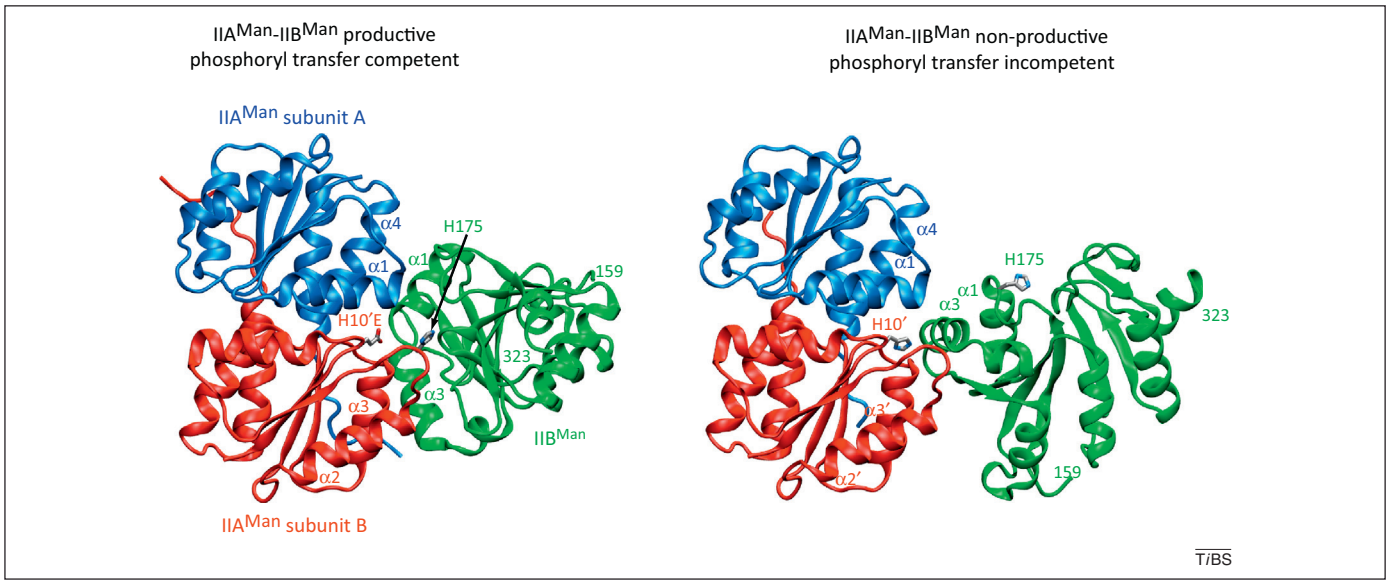

Figure 8. Productive, phosphoryl transfer competent (left) and nonproductive, phopshoryl transfer incompetent (right) complexes of IIA^{Man} and IIB^{Man}. Both productive and nonproductive complexes are significantly populated in the absence of phosphorylation or mutation of His10 of IIA^{Man} to Glu to mimic the phosphorylated state. The latter mutation shifts the equilibrium almost entirely to the productive complex. The two subunits of IIA^{Man} are shown in blue and red, respectively, and IIB^{Man} is in green. Only a single IIB^{Man} molecule is shown for clarity. Adapted from [20]. Abbreviations: IIA, Enzyme II domain A; IIB, Enzyme II domain B.

What is the possible role of the transient $HPr_{nonspecific}$/EIN/HPr ternary complexes? It is possible that these ternary complexes may help EI compete for the cellular pool of HPr, even while phosphotransfer is occurring at the EIN active site, thereby facilitating higher rates of sugar uptake when substrate is transiently abundant [79]. In other words, the ternary complexes may be important for efficiently reloading the EIN active site with HPr when demand for sugar transport is high. Given the intracellular concentrations of EI and HPr (5 and 20–100 μM, respectively), one can estimate that the population of ternary complex ensembles *in vivo* is ~1%. This estimate may be revised higher if intracellular crowding and compartmentalization further favors the formation of transient ternary complexes.

The IIA^{Man}–IIB^{Man} interaction provides an extreme example of a relatively long-lived, highly-populated (~50% occupancy) and well-defined encounter complex [20], as opposed to the invisible sparsely populated ensemble of transient states seen for the complexes of HPr with EI, IIA^{Mtl}, and IIA^{Man} [79,80]. In the case of IIA^{Man}–IIB^{Man}, the intermolecular NOE data report on a mixture of two species comprising a productive, phosphoryl transfer competent complex (Figure 8, left panel) and a nonproductive complex in which the two active site histidines (His10 of IIA^{Man} and His175 of IIB^{Man}) are separated by 25 Å (Figure 8, right panel). The productive and nonproductive complexes are in fast exchange with one another so that only a single set of resonances are observed, but the observed intermolecular NOEs are inconsistent with the existence of a single complex. The structural transition between productive and nonproductive complexes involves a 90° rotation coupled to a ~37 Å translation of IIB^{Man} relative to IIA^{Man}. The interaction surface, however, on IIA^{Man} for the nonproductive complex comprises a subset of residues located in the central region of the interface in the productive complex. Likewise, the interaction surfaces for the productive and nonproductive complexes on IIB^{Man} also partially overlap. Thus, the productive and nonproductive complexes are mutually exclusive, as are both of these complexes with the upstream IIA^{Man}–HPr complex.

The nonproductive IIA^{Man}–IIB^{Man} complex (or more accurately intermolecular NOEs attributable to the nonproductive complex) can be largely eliminated by introducing a phosphomimetic H10E mutation in IIA^{Man}. The equivalent phosphomimetic *His175E* in IIB^{Man}, however, has no effect. The selection of the productive complex by IIA^{Man}(H10E) can be attributed to charge neutralization through interaction of the negatively charged carboxylate of H10E (equivalent to phosphorylated His10) with the positively charged guanidino group of *Arg172* located at the center of the IIB^{Man} binding surface [20]. This is supported by mutation of *Arg172* to *Gln* which results in a substantial increase in the population of the productive complex; the nonproductive complex, however, is not completely eliminated as the mutation still leaves an unfavorable polar residue in the middle of the interface. These observations are consistent with the finding that IIB^{Man}(*R172Q*) is less efficiently phosphorylated than the wild type by IIA^{Man} [82].

What is the role of the nonproductive IIA^{Man}–IIB^{Man} complex? It could represent an extreme example of an encounter complex, where the nonproductive complex could facilitate formation of the specific complex in a similar manner as highly transient, diffuse encounter complex ensembles.

Concluding remarks

The complexes of the PTS provide a paradigm for studying protein–protein interactions and understanding the determinants of specificity in a multifaceted and complex signal transduction system that allows for interactions between many partner proteins. The complexes of the PTS, which range from ~30 to ~150 kDa, have also served as a framework for extending NMR methodology to larger and more complex systems, for establishing integrative hybrid

approaches combining RDCs and solution X-ray scattering to tackle systems in excess of 100 kDa, and for developing novel biophysical techniques based on NMR paramagnetic relaxation enhancement to uncover the existence of transient, spectroscopically invisible, sparsely populated encounter complexes that constitute the first step towards specific complex formation.

There remain two open questions/challenges that still need to be addressed with respect to the structural biology and biophysics of the PTS. The first relates to EI and the mechanism and dynamics of large interdomain structural rearrangements that must occur during the course of the catalytic cycle. How, for example, are small local structural changes in the EIC domain upon binding to PEP transmitted to the EIN domain? In the absence of PEP does the open free state coexit with a small population of spectroscopically invisible closed state (Figure 4), and if so, what is the population of the latter; what are the interconversion rates between the species; and how are these populations and rates modulated by different ligands (e.g., the substrate PEP versus the inhibitor α-ketoglutarate, both of which bind to the same site on EIC [28]). These questions can largely be addressed by multidimensional hetreonuclear NMR spectroscopy, including the application of relaxation dispersion and paramagnetic relaxation enhancement measurements, but are rendered especially challenging owing to the large size (by NMR standards) of EI. The second area relates to high-resolution structures of the transmembrane sugar transporters (IIC and IID; Figure 1) of the PTS, their interaction with Enzymes IIB, and the mechanism of selective sugar transport across the membrane. Although there have been some low-resolution electron microscopy (EM) and cysteine crosslinking studies on the IIC transporters from the glucose [83,84] and mannitol [85,86] branches, this field remains largely an open book. Encouragingly crystals of IIC^{Glc} diffracting to 4.5 Å resolution have been recently obtained [87]. Solving structures of the transmembrane transporters will require extensive biochemical work to obtain either crystals diffracting to high resolution or suitable preparations for single molecule analysis by EM.

Acknowledgments

G.M.C. thanks members of his laboratory, past and present, and colleagues who have made major contributions to the work on complexes of the PTS, in particular, D. Garrett, M. Cai, G. Wang, G. Cornilescu, D. Williams, J. Hu, K. Hu, J-Y. Suh, Y-S. Jung, C. Tang, J. Iwahara, Y. Takayama, A. Grishaev, and C. Schwieters. This work was supported by funds from the Intramural Program of the NIH, NIDDK, and the Intramural AIDS Targeted Antiviral Program of the Office of the Director of the NIH (to G.M.C.).

References

1 Kundig, W. *et al.* (1964) Phosphate bound to histidine in a protein as an intermediate in a novel phospho-transferase system. *Proc. Natl. Acad. Sci. U.S.A.* 52, 1067–1074
2 Meadow, N.D. *et al.* (1990) The bacterial phosphoenolpyruvate: glycose phosphotransferase system. *Annu. Rev. Biochem.* 59, 497–542
3 Postma, P.W. *et al.* (1993) Phosphoenolpyruvate: carbohydrate phosphotransferase systems of bacteria. *Microbiol. Rev.* 57, 543–594
4 Herzberg, O. and Klevit, R. (1994) Unraveling a bacterial hexose transport pathway. *Curr. Opin. Struct. Biol.* 4, 814–822
5 Robillard, G.T. and Broos, J. (1999) Structure/function studies on the bacterial carbohydrate transporters, enzymes II, of the phosphoenolpyruvate-dependent phosphotransferase system. *Biochim. Biophys. Acta* 1422, 73–104
6 Siebold, C. *et al.* (2001) Carbohydrate transporters of the bacterial phosphoenolpyruvate: sugar phosphotransferase system (PTS). *FEBS Lett.* 504, 104–111
7 Deutscher, J. *et al.* (2006) How phosphotransferase system-related protein phosphorylation regulates carbohydrate metabolism in bacteria. *Microbiol. Mol. Biol. Rev.* 70, 939–1031
8 Feese, M.D. *et al.* (1997) Structural studies of the *Escherichia coli* signal transducing protein IIA^{Glc}: implications for target recognition. *Biochemistry* 36, 16087–16096
9 Worthylake, D. *et al.* (1991) Three-dimensional structure of the *Escherichia coli* phosphocarrier protein III^{Glc}. *Proc. Natl. Acad. Sci. U.S.A.* 88, 10382–10386
10 Liao, D.I. *et al.* (1991) Structure of the IIA domain of the glucose permease of *Bacillus subtilis* at 2.2 Å resolution. *Biochemistry* 30, 9583–9594
11 van Montfort, R.L. *et al.* (1998) The structure of the *Escherichia coli* phosphotransferase $IIA^{mannitol}$ reveals a novel fold with two conformations of the active site. *Structure* 6, 377–388
12 Nunn, R.S. *et al.* (1996) Structure of the IIA domain of the mannose transporter from *Escherichia coli* at 1.7 Å resolution. *J. Mol. Biol.* 259, 502–511
13 Sliz, P. *et al.* (1997) The structure of enzyme $IIA^{lactose}$ from *Lactococcus lactis* reveals a new fold and points to possible interactions of a multicomponent system. *Structure* 5, 775–788
14 Tang, C. *et al.* (2005) Solution structure of enzyme $IIA^{Chitobiose}$ from the N,N′-diacetylchitobiose branch of the *Escherichia coli* phosphotransferase system. *J. Biol. Chem.* 280, 11770–11780
15 Legler, P.M. *et al.* (2004) Three-dimensional solution structure of the cytoplasmic B domain of the mannitol transporter $II^{mannitol}$ of the *Escherichia coli* phosphotransferase system. *J. Biol. Chem.* 279, 39115–39121
16 Suh, J.Y. *et al.* (2005) Visualization of the phosphorylated active site loop of the cytoplasmic B domain of the mannitol transporter $II^{Mannitol}$ of the *Escherichia coli* phosphotransferase system by NMR spectroscopy and residual dipolar couplings. *J. Mol. Biol.* 353, 1129–1136
17 van Montfort, R.L. *et al.* (1997) The structure of an energy-coupling protein from bacteria, $IIB^{cellobiose}$, reveals similarity to eukaryotic protein tyrosine phosphatases. *Structure* 5, 217–225
18 Ab, E. *et al.* (2001) NMR structure of cysteinyl-phosphorylated enzyme IIB of the N,N′-diacetylchitobiose-specific phosphoenolpyruvate-dependent phosphotransferase system of *Escherichia coli*. *J. Mol. Biol.* 308, 993–1009
19 Cai, M. *et al.* (2003) Solution structure of the phosphoryl transfer complex between the signal-transducing protein $IIA^{Glucose}$ and the cytoplasmic domain of the glucose transporter $IICB^{Glucose}$ of the *Escherichia coli* glucose phosphotransferase system. *J. Biol. Chem.* 278, 25191–25206
20 Hu, J. *et al.* (2008) Solution NMR structures of productive and non-productive complexes between the A and B domains of the cytoplasmic subunit of the mannose transporter of the *Escherichia coli* phosphotransferase system. *J. Biol. Chem.* 283, 11024–11037
21 Schauder, S. *et al.* (1998) Crystal structure of the IIB subunit of a fructose permease (IIB^{Lev}) from *Bacillus subtilis*. *J. Mol. Biol.* 276, 591–602
22 Orriss, G.L. *et al.* (2003) Crystal structure of the IIB^{Sor} domain of the sorbose permease from *Klebsiella pneumoniae* solved to 1.75 Å resolution. *J. Mol. Biol.* 327, 1111–1119
23 Seok, Y.J. *et al.* (1997) High affinity binding and allosteric regulation of *Escherichia coli* glycogen phosphorylase by the histidine phosphocarrier protein, HPr. *J. Biol. Chem.* 272, 26511–26521
24 Peterkofsky, A. *et al.* (1993) Bacterial adenylyl cyclases. *Prog. Nucleic Acids Res. Mol. Biol.* 44, 31–65
25 Novotny, M.J. *et al.* (1985) Allosteric regulation of glycerol kinase by enzyme III^{Glc} of the phosphotransferase system in *Escherichia coli* and *Salmonella typhimurium*. *J. Bacteriol.* 162, 810–816
26 Nam, T.W. *et al.* (2001) The *Escherichia coli* glucose transporter enzyme $IICB^{Glc}$ recruits the global repressor Mlc. *EMBO J.* 20, 491–498

27 Seitz, S. *et al.* (2003) Analysis of the interaction between the global regulator Mlc and EIIB^{Glc} of the glucose-specific phosphotransferase system in *Escherichia coli*. *J. Biol. Chem.* 278, 10744–10751
28 Venditti, V. *et al.* (2013) Structural basis for Enzyme I inhibition by α-ketoglutarate. *ACS Chem. Biol.* 8, 1232–1240
29 Doucette, C.D. *et al.* (2011) α-Ketoglutarate coordinates carbon and nitrogen utilization via enzyme I inhibition. *Nat. Chem. Biol.* 7, 894–901
30 Liao, D.I. *et al.* (1996) The first step in sugar transport: crystal structure of the amino terminal domain of enzyme I of the *E. coli* PEP: sugar phosphotransferase system and a model of the phosphotransfer complex with HPr. *Structure* 4, 861–872
31 Jia, Z. *et al.* (1993) The 2.0-A resolution structure of *Escherichia coli* histidine-containing phosphocarrier protein HPr. A redetermination. *J. Biol. Chem.* 268, 22490–22501
32 Herzberg, O. *et al.* (1992) Structure of the histidine-containing phosphocarrier protein HPr from *Bacillus subtilis* at 2.0-A resolution. *Proc. Natl. Acad. Sci. U.S.A.* 89, 2499–2503
33 Teplyakov, A. *et al.* (2006) Structure of phosphorylated enzyme I, the phosphoenolpyruvate:sugar phosphotransferase system sugar translocation signal protein. *Proc. Natl. Acad. Sci. U.S.A.* 103, 16218–16223
34 Marquez, J. *et al.* (2006) Structure of the full-length enzyme I of the phosphoenolpyruvate-dependent sugar phosphotransferase system. *J. Biol. Chem.* 281, 32508–32515
35 Oberholzer, A.E. *et al.* (2009) Crystal structure of enzyme I of the phosphoenolpyruvate sugar phosphotransferase system in the dephosphorylated state. *J. Biol. Chem.* 284, 33169–33176
36 Wittekind, M. *et al.* (1992) Solution structure of the phosphocarrier protein HPr from *Bacillus subtilis* by two-dimensional NMR spectroscopy. *Protein Sci.* 1, 1363–1376
37 van Nuland, N.A.J. *et al.* (1994) The high-resolution structure of the histidine-containing phosphocarrier protein HPr from *Escherichia coli* determined by restrained molecular dynamics from nuclear magnetic resonance nuclear Overhauser effect data. *J. Mol. Biol.* 237, 544–559
38 van Nuland, N.A.J. *et al.* (1995) High-resolution structure of the phosphorylated form of the histidine-containing phosphocarrier protein HPr from *Escherichia coli* determined by restrained molecular dynamics from NMR NOE data. *J. Mol. Biol.* 246, 180–193
39 Garrett, D.S. *et al.* (1997) Solution structure of the 30 kDa N-terminal domain of enzyme I of the *Escherichia coli* phosphoenolpyruvate:sugar phosphotransferase system by multidimensional NMR. *Biochemistry* 36, 2517–2530
40 Schwieters, C.D. *et al.* (2010) Solution structure of the 128 kDa enzyme I dimer from *Escherichia coli* and its 146 kDa complex with HPr using residual dipolar couplings and small- and wide-angle X-ray scattering. *J. Am. Chem. Soc.* 132, 13026–13045
41 Takayama, Y. *et al.* (2011) Combined use of residual dipolar couplings and solution X-ray scattering to rapidly probe rigid-body conformational transitions in a non-phosphorylatable active-site mutant of the 128 kDa enzyme I dimer. *J. Am. Chem. Soc.* 133, 424–427
42 Garrett, D.S. *et al.* (1999) Solution structure of the 40,000 M_r phosphoryl transfer complex between the N-terminal domain of enzyme I and HPr. *Nat. Struct. Biol.* 6, 166–173
43 Clore, G.M. (2000) Accurate and rapid docking of protein-protein complexes on the basis of intermolecular nuclear overhauser enhancement data and dipolar couplings by rigid body minimization. *Proc. Natl. Acad. Sci. U.S.A.* 97, 9021–9025
44 Schwieters, C.D. and Clore, G.M. (2001) Internal coordinates for molecular dynamics and minimization in structure determination and refinement. *J. Magn. Reson.* 152, 288–302
45 Cornilescu, G. *et al.* (2002) Solution structure of the phosphoryl transfer complex between the cytoplasmic A domain of the mannitol transporter II^{Mannitol} and HPr of the *Escherichia coli* phosphotransferase system. *J. Biol. Chem.* 277, 42289–42298
46 Clore, G.M. and Gronenborn, A.M. (1998) Determining the structures of large proteins and protein complexes by NMR. *Trends Biotechnol.* 16, 22–34
47 Wang, G. *et al.* (2000) Solution structure of the phosphoryl transfer complex between the signal transducing proteins HPr and IIA^{glucose} of the *Escherichia coli* phosphoenolpyruvate:sugar phosphotransferase system. *EMBO J.* 19, 5635–5649
48 Williams, D.C., Jr *et al.* (2005) Solution NMR structure of the 48-kDa IIA^{Mannose}-HPr complex of the *Escherichia coli* mannose phosphotransferase system. *J. Biol. Chem.* 280, 20775–20784
49 Jung, Y.S. *et al.* (2012) Solution structure of the IIA^{Chitobiose}-HPr complex of the N,N′-diacetylchitobiose branch of the *Escherichia coli* phosphotransferase system. *J. Biol. Chem.* 287, 23819–23829
50 Suh, J.Y. *et al.* (2006) Solution structure of a post-transition state analog of the phosphotransfer reaction between the A and B cytoplasmic domains of the mannitol transporter II^{Mannitol} of the *Escherichia coli* phosphotransferase system. *J. Biol. Chem.* 281, 8939–8949
51 Jung, Y.S. *et al.* (2010) Solution structure of the IIA^{Chitobiose}-IIB^{Chitobiose} complex of the N,N′-diacetylchitobiose branch of the *Escherichia coli* phosphotransferase system. *J. Biol. Chem.* 285, 4173–4184
52 Nam, T.W. *et al.* (2008) Analyses of Mlc-IIB^{Glc} interaction and a plausible molecular mechanism of Mlc inactivation by membrane sequestration. *Proc. Natl. Acad. Sci. U.S.A.* 105, 3751–3756
53 Herzberg, O. (1992) An atomic model for protein-protein phosphoryl group transfer. *J. Biol. Chem.* 267, 24819–24823
54 Begley, G.S. *et al.* (1982) Stereochemical course of the reactions catalyzed by the bacterial phosphoenolpyruvate:glucose phosphotransferase system. *Biochemistry* 21, 5552–5556
55 Mueller, E.G. *et al.* (1990) Stereochemical course of the reactions catalyzed by the bacterial phosphoenolpyruvate:mannitol phosphotransferase system. *Biochemistry* 29, 6892–6896
56 Hollfelder, F. and Herschlag, D. (1995) The nature of the transition state for enzyme-catalyzed phosphoryl transfer. Hydrolysis of O-aryl phosphorothioates by alkaline phosphatase. *Biochemistry* 34, 12255–12264
57 Rohwer, J.M. *et al.* (2000) Understanding glucose transport by the bacterial phosphoenolpyruvate:glycose phosphotransferase system on the basis of kinetic measurements *in vitro*. *J. Biol. Chem.* 275, 34909–34921
58 Suh, J.Y. *et al.* (2007) Intramolecular domain-domain association/dissociation and phosphoryl transfer in the mannitol transporter of *Escherichia coli* are not coupled. *Proc. Natl. Acad. Sci. U.S.A.* 104, 3153–3158
59 Northrup, S.H. and Erickson, H.P. (1992) Kinetics of protein-protein association explained by Brownian dynamics computer simulation. *Proc. Natl. Acad. Sci. U.S.A.* 89, 3338–3342
60 Meadow, N.D. and Roseman, S. (1982) Sugar transport by the bacterial phosphotransferase system. Isolation and characterization of a glucose-specific phosphocarrier protein (III^{Glc}) from *Salmonella typhimurium*. *J. Biol. Chem.* 257, 14526–14537
61 Meadow, N.D. *et al.* (1986) Limited proteolysis of III^{Glc}, a regulatory protein of the phosphoenolpyruvate:glycose phosphotransferase system, by membrane-associated enzymes from *Salmonella typhimurium* and *Escherichia coli*. *J. Biol. Chem.* 261, 13504–13509
62 Wang, G. *et al.* (2000) A novel membrane anchor function for the N-terminal amphipathic sequence of the signal-transducing protein IIA^{Glucose} of the Escherichia coli phosphotransferase system. *J. Biol. Chem.* 275, 39811–39814
63 Chauvin, F. *et al.* (1996) The N-terminal domain of *Escherichia coli* enzyme I of the phosphoenolpyruvate/glycose phosphotransferase system: molecular cloning and characterization. *Proc. Natl. Acad. Sci. U.S.A.* 93, 7028–7031
64 Chauvin, F. *et al.* (1996) Enzyme I: the first protein and potential regulator of the bacterial phosphoenolpyruvate: glycose phosphotransferase system. *Res. Microbiol.* 147, 471–479
65 Saier, M.H., Jr *et al.* (1980) Phosphoryl exchange reaction catalyzed by enzyme I of the bacterial phosphoenolpyruvate: sugar phosphotransferase system. Kinetic characterization. *J. Biol. Chem.* 255, 8579–8584
66 Meadow, N.D. *et al.* (2005) Transient state kinetics of Enzyme I of the phosphoenolpyruvate:glycose phosphotransferase system of *Escherichia coli*: equilibrium and second-order rate constants for the phosphotransfer reactions with phosphoenolpyruvate and HPr. *Biochemistry* 44, 12790–12796
67 Oberholzer, A.E. *et al.* (2005) Crystal structure of the phosphoenolpyruvate-binding enzyme I-domain from the *Thermoanaerobacter tengcongensis* PEP: sugar phosphotransferase system (PTS). *J. Mol. Biol.* 346, 521–532

68 Navdaeva, V. *et al.* (2011) Phosphoenolpyruvate: sugar phosphotransferase system from the hyperthermophilic *Thermoanaerobacter tengcongensis*. *Biochemistry* 50, 1184–1193
69 Patel, H.V. *et al.* (2006) Properties of the C-terminal domain of enzyme I of the *Escherichia coli* phosphotransferase system. *J. Biol. Chem.* 281, 17579–17587
70 Patel, H.V. *et al.* (2006) The monomer/dimer transition of enzyme I of the *Escherichia coli* phosphotransferase system. *J. Biol. Chem.* 281, 17570–17578
71 Venditti, V. and Clore, G.M. (2012) Conformational selection and substrate binding regulate the monomer/dimer equilibrium of the C-terminal domain of *Escherichia coli* enzyme I. *J. Biol. Chem.* 287, 26989–26998
72 Gabdoulline, R.R. and Wade, R.C. (2002) Biomolecular diffusional association. *Curr. Opin. Struct. Biol.* 12, 204–213
73 Schreiber, G. *et al.* (2009) Fundamental aspects of protein-protein association kinetics. *Chem. Rev.* 109, 839–860
74 Blundell, T.L. and Fernandez-Recio, J. (2006) Cell biology: brief encounters bolster contacts. *Nature* 444, 279–280
75 Northrup, S.H. *et al.* (1988) Brownian dynamics of cytochrome c and cytochrome c peroxidase association. *Science* 241, 67–70
76 Schreiber, G. and Fersht, A.R. (1996) Rapid, electrostatically assisted association of proteins. *Nat. Struct. Biol.* 3, 427–431
77 Zhou, H.X. and Szabo, A. (2004) Enhancement of association rates by nonspecific binding to DNA and cell membranes. *Phys. Rev. Lett.* 93, 178101
78 Harel, M. *et al.* (2007) On the dynamic nature of the transition state for protein-protein association as determined by double-mutant cycle analysis and simulation. *J. Mol. Biol.* 371, 180–196
79 Fawzi, N.L. *et al.* (2010) Mechanistic details of a protein-protein association pathway revealed by paramagnetic relaxation enhancement titration measurements. *Proc. Natl. Acad. Sci. U.S.A.* 107, 1379–1384
80 Tang, C. *et al.* (2006) Visualization of transient encounter complexes in protein-protein association. *Nature* 444, 383–386
81 Suh, J.Y. *et al.* (2007) Role of electrostatic interactions in transient encounter complexes in protein-protein association investigated by paramagnetic relaxation enhancement. *J. Am. Chem. Soc.* 129, 12954–12955
82 Gutknecht, R. *et al.* (1998) Mutational analysis of invariant arginines in the IIAB(Man) subunit of the *Escherichia coli* phosphotransferase system. *J. Biol. Chem.* 273, 12234–12238
83 Koch, M.H. *et al.* (2003) Small-angle scattering: a view on the properties, structures and structural changes of biological macromolecules in solution. *Q. Rev. Biophys.* 36, 147–227;
Zhuang, J. *et al.* (1999) Purification and electron microscopic characterization of the membrane subunit ($IICB^{Glc}$) of the *Escherichia coli* glucose transporter. *Arch. Biochem. Biophys.* 372, 89–96
84 Jeckelmann, J.M. *et al.* (2011) Structure and function of the glucose PTS transporter from *Escherichia coli*. *J. Struct. Biol.* 176, 395–403
85 Koning, R.I. *et al.* (1999) The 5 Å projection structure of the transmembrane domain of the mannitol transporter enzyme II. *J. Mol. Biol.* 287, 845–851
86 van Montfort, B.A. *et al.* (2001) Cysteine cross-linking defines part of the dimer and B/C domain interface of the *Escherichia coli* mannitol permease. *J. Biol. Chem.* 276, 12756–12763
87 Zurbriggen, A. *et al.* (2010) Expression, purification, crystallization and preliminary X-ray analysis of the $EIIC^{Glc}$ domain of the *Escherichia coli* glucose transporter. *Acta Crystallogr. Sect. F: Struct. Biol. Cryst. Commun.* 66, 684–688
88 Grishaev, A. *et al.* (2005) Refinement of multidomain protein structures by combination of solution small-angle X-ray scattering and NMR data. *J. Am. Chem. Soc.* 127, 16621–16628
89 Grishaev, A. *et al.* (2008) Refined solution structure of the 82-kDa enzyme malate synthase G from joint NMR and synchrotron SAXS restraints. *J. Biomol. NMR* 40, 95–106
90 Schwieters, C.D. and Clore, G.M. (2007) A physical picture of atomic motions within the Dickerson DNA dodecamer in solution derived from joint ensemble refinement against NMR and large-angle X-ray scattering data. *Biochemistry* 46, 1152–1166
91 Clore, G.M. and Gronenborn, A.M. (1991) Structures of larger proteins in solution: three- and four-dimensional heteronuclear NMR spectroscopy. *Science* 252, 1390–1399
92 Clore, G.M. and Gronenborn, A.M. (1998) New methods of structure refinement for macromolecular structure determination by NMR. *Proc. Natl. Acad. Sci. U.S.A.* 95, 5891–5898
93 Bax, A. *et al.* (1994) Measurement of homo- and heteronuclear J couplings from quantitative J correlation. *Methods Enzymol.* 239, 79–105
94 Shen, Y. *et al.* (2009) TALOS+: a hybrid method for predicting protein backbone torsion angles from NMR chemical shifts. *J. Biomol. NMR* 44, 213–223
95 Prestegard, J.H. *et al.* (2000) NMR structures of biomolecules using field oriented media and residual dipolar couplings. *Q. Rev. Biophys.* 33, 371–424
96 Clore, G.M. and Garrett, D.S. (1999) R-factor, free R, and complete cross-validation for dipolar coupling refinement of NMR structures. *J. Am. Chem. Soc.* 121, 9008–9012
97 Tjandra, N. and Bax, A. (1997) Direct measurement of distances and angles in biomolecules by NMR in a dilute liquid crystalline medium. *Science* 278, 1111–1114
98 Clore, G.M. *et al.* (1998) Measurement of residual dipolar couplings of macromolecules aligned in the nematic phase of a colloidal suspension of rod-shaped viruses. *J. Am. Chem. Soc.* 120, 10571–10572
99 Iwahara, J. and Clore, G.M. (2006) Detecting transient intermediates in macromolecular binding by paramagnetic NMR. *Nature* 440, 1227–1230
100 Clore, G.M. and Iwahara, J. (2009) Theory, practice, and applications of paramagnetic relaxation enhancement for the characterization of transient low-population states of biological macromolecules and their complexes. *Chem. Rev.* 109, 4108–4139